

# Quantum sensing of time dependent electromagnetic fields with single electron excitations

H. Souquet-Basiège<sup>1</sup>, B. Roussel<sup>2</sup>, G. Reborá<sup>1</sup>, G. Menard<sup>4</sup>, I. Safi<sup>3</sup>, G. Fève<sup>4</sup>, and P. Degiovanni<sup>1</sup>

(1) *Univ Lyon, Ens de Lyon, Université Claude Bernard Lyon 1, CNRS, Laboratoire de Physique, F-69342 Lyon, France*

(2) *Departement of Applied Physics, Aalto University, 00076 Aalto, Finland*

(3) *Laboratoire de Physique des Solides (UMR 5802),*

*CNRS-Université Paris-Sud and Paris-Saclay, Bâtiment 510, 91405 Orsay, France and*

(4) *Laboratoire de Physique de l'École Normale Supérieure, ENS, Université PSL, CNRS, Sorbonne Université, Université de Paris, F-75005 Paris, France*

In this study, we investigate the potential of electronic interferometers for probing the quantum state of electromagnetic radiation on a chip at sub-nanosecond time scales. We propose to use single electron excitations propagating within an electronic Mach-Zehnder interferometer in the Aharonov-Bohm dominated regime. We discuss how information about the quantum state of the electromagnetic radiation is encoded into the interference contribution to the average outgoing electrical current. By investigating squeezed radiation and single edge magnetoplasmons probed by Leviton pulses in a realistic setup, we show that single electron interferometers have the potential to probe quantum radiation in the time domain with sub-nanosecond to pico-second time resolution. Our research could have significant implications for probing the fundamental properties of light in the microwave to tera-Hertz domains at extremely short time scales.

PACS numbers: 73.23.-b, 73.43.-f, 71.10.Pm, 73.43.Lp

Keywords: quantum Hall effect, quantum sensing, decoherence

## I. INTRODUCTION

Initiated by the demonstration of on-demand single electron sources in quantum Hall edge channels [1, 2], electron quantum optics (EQO) [3] has seen the demonstration of several important milestones such as electronic Hanbury Brown and Twiss (HBT) [4], Hong Ou Mandel (HOM) [5] experiments, quantitative studies of electronic decoherence using HOM [6] and Mach Zehnder interferometry [7–11]. More recently, a full characterization of the quantum state and coherences of single electron and hole excitations within a quantum Hall edge channel has been performed [12]. By demonstrating our ability to access electronic quantum states in a quantum conductor at an unprecedented level, these achievements strongly suggest that EQO is now mature for exploring its applications. The extreme sensitivity of individual electronic excitations to their electromagnetic environment suggests to explore the potential of EQO for the sensing of electromagnetic fields at the  $\mu\text{m}$  spatial scale and down to a few ps time scale [13].

This would be of great interest in the current effort to extend the paradigms of quantum coherent nano-electronics to higher frequencies, possibly up to the THz range [14] since the electromagnetic wavelength (mm) is still much larger than the size of the device (from 1 to few tens of  $\mu\text{m}$ ). For example, interferometric detection of a single electron at sub-nanosecond time scale is indeed instrumental in a recent proposal for single shot detection of an electronic flying qubit [15]. In a broader perspective, solid state systems envisioned for quantum technolo-

gies [16–18] involve quantum electromagnetic fields in the GHz to THz range. Quantum optics in the THz domain also offers interesting perspectives for studying quantum materials [19]. This calls for sensors that can probe the properties of these fields on the chip and at such short time scales.

However, sensing and analyzing of local quantum electric fields on very short time scales is notoriously difficult. Rydberg atoms based quantum electrometers [20] have reached record sensitivities but for static fields. Fast electrical modulation of optical systems enables measuring the electric field up to a THz-bandwidth [21]. Unfortunately, such optical systems are not suitable for quantum mesoscopic devices due to the difficulty of combining optics and microwave electronics within the same cryostat and the large size of the sensing area. On-chip systems based on nano-mechanical resonators [22, 23], rf-capacitive gate based sensing [24], NV-centers in diamond [25] as well as quantum dots [26, 27] have been demonstrated, often as charge sensors able to detect a single electron charge at a few tens of nm. But their bandwidth is still limited to 1 to 10 MHz at best, obtained with rf-SETs [28], Quantum Point Contacts (QPCs) [29], rf-SQUIDS [30] or quantum dots [31]. Moreover, they are not designed to detect quantum features of the electromagnetic field such as non-classical fluctuations.

In this paper, we discuss the electron quantum radar (EQR) as a way to probe the quantum state of an electromagnetic radiation using a single electron interferometer. This idea is dual to the one underlying radars and coherent lidars which are electromagnetic interferometers probing a material target. Here, the “Electron Quantum

Radar” (EQR) is an electronic Mach-Zehnder interferometer (MZI) [32] where one branch is capacitively coupled to a radiation channel in which the external electromagnetic radiation propagates as depicted on Fig. 1. The EQR obtains information on the quantum state of the radiation by comparing ballistic propagation within the “reference branch” of the MZI and propagation in the “target branch” coupled to the radiation. This is different from the proposal of Ref. [33] in which non-classical radiation is probed via photo-assisted tunneling. It is closer to an interferometric probe of a quantum electromagnetic field by matter [34] although, here, it is not a quantum non-demolition measurement since the coupling operator is a quadrature of the field [35].

As shown in the present work, single electron excitations are the most promising probes of quantum radiation involving single to a few photons because the associated quantum electrical current generates a very small back-action on this radiation compared to electrical currents involving more electronic excitations. Moreover, the demonstration of single electron tomography protocols [12, 36, 37] supplemented by quantum current analysis algorithms [38] as well as the generation of wave packets in the tens to few ps range in a variety of systems [14, 39–42] suggest that the versatility of single electron sources may enable us to probe properties of quantum radiation both in the time and frequency domains. Most importantly, a Levitonic MZI has recently been demonstrated in graphene [43].

Motivated by this perspective, a full theory of the single electron quantum radar is presented here. The central result of this paper is the single electron radar equation which gives the interference contribution to the average electrical current in terms of the electronic single electron wave-packet and the quantum state of the electromagnetic radiation. All the dynamics is contained in the linear response properties of the “radiation coupler” coupling the target branch to the radiation.

This equation accounts for the interferometer’s back action on the incident radiation, which leads to electronic decoherence [44, 45]. We show that all information about the state of the incident quantum radiation is contained in a Franck-Condon recoil factor [46] describing the change of the incident radiation upon the propagation of a time resolved single electron excitation across the interferometer. This result is established using the plasmon scattering matrix related to finite frequency admittances [47, 48] to describe the coupling between the external radiation and the plasmon modes within the target branch of the MZI.

In the case of a classical radiation, this recoil factor includes a pure phase corresponding to the classical electrical potential seen by the electron during its propagation. When the quantum state of the incident quantum radiation is Gaussian, this recoil factor captures the time-dependent fluctuations in the mode selected by the capacitive coupling between the radiation and the electrons. This enables us to give an operational criterion to

test if the fluctuations are sub-vacuum. This result may be of interest in the light of recent theoretical [49, 50] and experimental [51] studies of squeezing in quantum Hall edge channels as well as in tunnel junctions [52, 53]. As a last example, we discuss the electron radar signature of single to few edge magnetoplasmons (EMPs) propagating in a nearby quantum Hall edge channel and show that, when the radiation coupler provides a broadband filtering of the incoming radiation, the recoil factor in the time domain is proportional to the instantaneous average heat current [54] carried by a single EMP.

This paper is structured as follows: Sec. II presents the basic ideas for sensing classical or quantum electromagnetic fields with an electronic interferometer. In particular, we show the importance of the back-action of the interferometer when probing quantum electromagnetic radiation. The theory of a single electron Mach-Zehnder interferometer with one of its branch irradiated by a quantum electromagnetic field is then presented in Sec. III and its core result – the single electron radar equation – is derived. Explicit predictions for classical and quantum radiation (squeezed and Fock states) probed by Levitons are presented in Sec. IV.

## II. SENSING ELECTROMAGNETIC FIELDS WITH ELECTRONS

In this section, we discuss the physics of the electronic MZI as a probe of an external radiation at a qualitative level. Secs. II A and II B are devoted to estimating the classical phase shift induced on the probing electron in the radiation-coupler (or radiation coupler) by a nearby propagating single electron current and then a classical time dependent voltage. Then, in Sec. II C, we consider an incident quantum radiation and we show that, to avoid decoherence effects, a compromise must be found on the strength of the electron/radiation coupling. The discussion of back-action effects also explains why single electron interferometry is appropriate for probing the quantum state of mesoscopic quantum radiation involving a low average number of photons.

### A. Electromagnetic phase shifts

Before modeling the MZI, let us estimate the order of magnitude of the phase shift induced by a nearby electron on the electron propagating within the MZI. In Ref. [13], a “small electron collider” depicted on Fig. 2 has been considered. The phase shift  $\delta\phi_{\text{coll}}$  associated with Coulomb potential for electrons flying nearby each other at velocity  $v_F$  is, up to some geometric factor, of the order of the effective fine structure constant within the

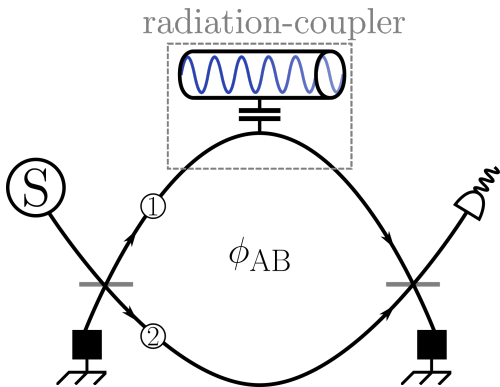


FIG. 1. Scheme of principle for sensing electromagnetic fields with single electron excitations. An electronic Mach-Zehnder interferometer (MZI) is formed by combining two quantum point contacts  $A$  and  $B$  acting as ideal electronic beam splitter. It encloses a magnetic flux  $\Phi_B$  inducing an Aharonov-Bohm phase  $\phi_{AB} = e\Phi_B/\hbar$ . The interferometer is fed by a single electron source  $S$  located right before the first beam splitter  $A$ . One measures the Aharonov-Bohm flux dependent part of the average outgoing electrical current  $\langle i_{1\text{out}}(t) \rangle$  or  $\langle \tilde{i}_{1\text{out}}(\omega) \rangle$ . The branch 1 is capacitively coupled to external electromagnetic radiation.

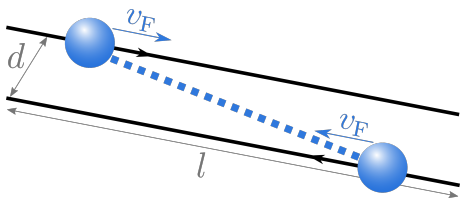


FIG. 2. Collision of two electrons propagating within two counter-propagating 1D channels at velocity  $v_F$ , separated by a distance  $d$  and feeling Coulomb potential within a region of length  $l$  in a dielectric material of relative permittivity  $\epsilon_r$ .

material

$$\delta\phi_{\text{coll}} = \alpha_{\text{eff}} \operatorname{arcsinh}(l/d) \quad (1a)$$

$$\alpha_{\text{eff}} = \frac{e^2}{4\pi\epsilon_0\epsilon_r\hbar v_F} = \frac{\alpha_{\text{qed}}}{\epsilon_r} \frac{c}{v_F} \quad (1b)$$

For AlGaAs/AsGa with relative permittivity  $\epsilon_r = 12.9$  and a typical Fermi velocity  $v_F = 10^5 \text{ ms}^{-1}$ ,  $\alpha_{\text{eff}} \sim 1.7$  and therefore, for  $l = 1 \mu\text{m}$  and  $d = 100 \text{ nm}$ ,  $\delta\phi_{\text{coll}}/2\pi \simeq 0.81$  which is not small compared to unity. Similar phase estimates have also been discussed in two-electron collision within an HOM interferometer [55].

This estimate suggests that, using the typical radiation coupler geometry depicted on Fig. 1, a single electron excitation propagating within the MZI may be able to detect the time dependent electromagnetic field associated with a single electron passing by in the radiation channel.

## B. Sensing a classical voltage drive

To understand how the shape of the probing electron's wave packet influences its detection capabilities, we now discuss more precisely the behaviour of the single electron MZI depicted on Fig. 1 using single-particle physics.

Two quantum point contacts (QPC) behave as ideal electronic beam splitters with scattering matrices

$$S_\alpha = \begin{pmatrix} \sqrt{T_\alpha} & i\sqrt{R_\alpha} \\ i\sqrt{R_\alpha} & \sqrt{T_\alpha} \end{pmatrix} \quad (2)$$

for  $\alpha = A$  or  $\alpha = B$  where  $T_\alpha$  and  $R_\alpha$  are the transmission and reflection probabilities ( $T_\alpha + R_\alpha = 1$ ). A static perpendicular magnetic field  $B$  is applied, generating an Aharonov-Bohm phase  $\phi_{AB}$  enclosed between the arms 1 and 2.

We assume that electrons feel a time dependent classical potential  $U(t)$  along branch 1 and propagate ballistically along branch 2 with time of flight  $\tau_2$ . The amplitude for a single electron to enter into branch 1 at time  $t'$  and arrive at the second beam splitter at time  $t$  is then given by

$$R(t, t') = \delta(t - t' - \tau_1) e^{\frac{ie}{\hbar} \int_{t'}^t U(\tau) d\tau} \quad (3)$$

in which  $\tau_1$  denotes the ballistic time of flight across branch 1. The prefactor is the electric phase accumulated by the electron during its propagation. We can then compute the probability for an electron emitted by source  $S$  in a single particle state  $\varphi_e$  to be detected in the outgoing branch 1:

$$p(1_{\text{out}}) = R_A R_B + T_A T_B + \mathcal{P}_q \quad (4)$$

in which the quantum interference contribution  $\mathcal{P}_q$  is given by

$$\mathcal{P}_q = \mathcal{K} \Re \left( e^{i\phi_{AB}} \int_{\mathbb{R}} \varphi_e(t - \tau_1) e^{\frac{ie}{\hbar} \int_{t-\tau_1}^t U(\tau) d\tau} \varphi_e(t - \tau_2)^* dt \right) \quad (5)$$

where  $\mathcal{K} = \sqrt{R_A R_B T_A T_B}$ . In the limit of a very short electronic wave packet emitted at time  $t_e$  and for  $\tau_1 = \tau_2$  we obtain

$$\mathcal{P}_q \propto \Re \left( e^{i\phi_{AB}} e^{i\delta\phi_U(t_e)} \right) \quad (6)$$

where the phase

$$\delta\phi_U(t_e) = \frac{e}{\hbar} \int_{t_e}^{t_e + \tau_1} U(\tau) d\tau \quad (7)$$

is the electric phase accumulated during the time interval  $[t_e, t_e + \tau_1]$ . This result corresponds to our intuition from optics: the interferometer provides a way to access the phase difference between the two propagation paths which, in the present case, is directly related to the classical voltage experienced by the electrons during their propagation along branch 1.

In order to discuss how an electronic MZI can be used to probe the quantum state of a radiation, a quantum description of the radiation/electron coupling is needed.

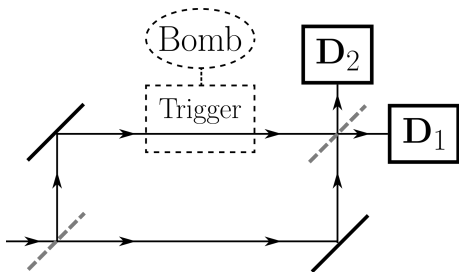


FIG. 3. The Elitzur-Vaidman’s interferometer: in the absence of the bomb, this single photon Mach-Zehnder interferometer is calibrated so that there is no click in  $D_2$ . In the presence of the bomb, the trigger absorbs an incident photon with 100% efficiency and detonates the bomb. Interferences are destroyed and there is a probability 1/4 for the traveling particles to be detected by  $D_2$ .

### C. Interferometric sensing of a quantum system

The simplest way to understand how a quantum interferometer can probe the state of a quantum system coupled to one of its branches is to discuss a generalization of the Elitzur-Vaidman bomb detector [56].

In this work, a quantum interferometer is used to detect the presence of a bomb without triggering its explosion. The bomb’s trigger is activated as soon as a particle travels across branch 1 of the interferometer (see Fig. 3). This assumes that the bomb’s trigger is a perfectly efficient particle detector. The idea is then to tune the optical paths of the MZI so that, in the absence of the bomb, the particle exits on one of its outgoing branch but not in the other. In the presence of the bomb, the particle exits with probability 1/4 in the branch where it would never exit in the absence of the bomb. This provides a sure diagnostic of its presence without interacting with its trigger, hence the commonly used term “interaction free measurement” to describe this process.

However, in the present context, we are interested into exploiting the interaction between the particle and the bomb’s trigger to gain information not only about its presence of absence but also about its quantum state.

The bomb initially being in the  $|\text{Idle}\rangle$  state, interaction with the incident photon leads to an entangled state involving two alternatives: first, as in Elitzur and Weidman’s work, when the photon is absorbed, the bomb is detonated. But we also account for a fizzling of the bomb in which the photon is not absorbed although its quantum state can be altered. The full interaction between the particle and the bomb is then described by the quantum coherent process

$$|\Psi\rangle \otimes |\text{Idle}\rangle \longrightarrow \mathcal{A}_0 |\emptyset\rangle \otimes |\text{Detonated}\rangle + \mathcal{A}_1 |\Psi'\rangle \otimes |\text{Fizzled}\rangle \quad (8a)$$

in which  $|\emptyset\rangle$  denotes the vacuum state (the particle has been absorbed) and  $|\Psi'\rangle$  the modified state of the photon in case of fizzling. The Elitzur-Vaidman interaction free

measurement corresponds to  $|\mathcal{A}_0|^2 = 1$  but, here both alternatives are allowed and thus  $|\mathcal{A}_0|^2 + |\mathcal{A}_1|^2 = 1$ . For balanced beam splitters, the conditional output probabilities are then given by the following expressions :

$$p(\text{No Particle}) = \frac{1}{2}(1 - |\mathcal{A}_1|^2) \quad (9a)$$

$$p(1_{\text{out}}) = \frac{1}{4}(1 + |\mathcal{A}_1|^2) - \mathcal{P}_q \quad (9b)$$

$$p(2_{\text{out}}) = \frac{1}{4}(1 + |\mathcal{A}_1|^2) + \mathcal{P}_q \quad (9c)$$

in which quantum interference effects are contained in

$$\mathcal{P}_q = \frac{1}{2} \Re(\mathcal{A}_1 e^{i\phi_{AB}} \langle \text{Idle} | \text{Fizzled} \rangle \langle \Psi | \Psi' \rangle) \quad (10)$$

which is sensitive to the (Aharonov-Bohm) phase difference  $\phi_{AB}$  associated with free propagation along the two branches of the MZI. Information on the quantum state of the bomb is contained in the product of the two overlaps  $\langle \Psi | \Psi' \rangle$  and  $\langle \text{Idle} | \text{Fizzled} \rangle$ .

From our perspective, the bomb plays the role of the incoming electromagnetic radiation and the particle is the quantum electrical current propagating within the MZI. The process in which the particle is absorbed and the bomb is detonated corresponds to a full electronic decoherence within the MZI. It occurs whenever Coulomb interactions lead to the generation of any extra electron/hole pair within the channel 1 of the MZI compared to ballistic propagation along channel 2. The resulting many-body state will then have a vanishing overlap with the ballistic propagation of a single electron excitation within branch 2 of the MZI. However, this is not the case of interest for the electron radar since, in this case, the interference contribution to the average current vanishes and, as in the Elitzur-Vaidman case, nothing can be learned on the quantum state of the incoming radiation.

By contrast, in the absence of generation of extra electron/hole pair particles, the state of the electron propagating within branch 1 is altered by its coupling to the incoming radiation: this corresponds to the change  $|\Psi\rangle \mapsto |\Psi'\rangle$  in the above discussion. For a classical radiation, this is the phase shift associated with the voltage experienced by the electrons (see Sec. II B).

The alteration of the bomb’s state  $|\text{Idle}\rangle \mapsto |\text{Fizzled}\rangle$  in the above discussion corresponds to the effect of the propagating electron on the incident radiation in the situation where no extra-electron/hole pairs are created. This is the back action of the interferometer, seen as a measurement device, on the radiation. The amplitude  $\langle \text{Idle} | \text{Fizzled} \rangle$  that measure the “quantum recoil” of the radiation upon propagation of a single electron without generating extra electron/hole pairs along branch 1 of the MZI. As we shall see in Sec. III, this is precisely the part that will contain information on the quantum fluctuations of the incoming radiation.

When the back-action is too important, the overlap  $\langle \text{Idle} | \text{Fizzled} \rangle$  may vanish and the interference signal is then lost. This point explains why quantum electrical

currents carrying a single electronic excitations are relevant for probing mesoscopic quantum electromagnetic fields which involve a low average number of photons: besides decoherence which is generically less important for them, single electron currents lead to a smaller back-action than currents carrying more excitations.

In the end, this qualitative discussion suggests that, extracting information on the incoming radiation thus requires a compromise: electronic decoherence as well as back-action on the quantum radiation has to be moderate to ensure an experimentally accessible experimental signal but strong enough to ensure sensitivity to the incoming quantum radiation.

### III. THE SINGLE ELECTRON RADAR THEORY

In this section, we derive the central result of this work which is the single electron radar equation expressing the interference contribution to the outgoing average current in terms of two distinct quantities: firstly, the excess single electron coherence of the injected wave packet which depends only on the electronic source  $S$ . Secondly, an effective single particle scattering amplitude describing both the effects of electronic decoherence and of the incoming radiation. The latter quantity reflects the dynamics of the interferometer coupled to its electromagnetic environment.

Although this result is formally derived in Appendix E using bosonization of chiral quantum Hall edge channels, a more intuitive derivation is presented in Secs. III A and III B.

#### A. Radiation coupler modeling

The radiation coupler involves a capacitive coupling between a portion of the upper branch of the electronic MZI and the external radiation channel which is fed by the incoming electromagnetic radiation we want to study. Effect of Coulomb interactions within this region will be described within the framework of edge-magnetoplasmon scattering. Originally introduced in the context of finite frequency quantum transport in 1D [47, 48, 57], it enables us to describe the scattering between the EMP modes propagating along the MZI edge channel and the bosonic modes within the external radiation channel [58].

For simplicity, we assume that the whole upper branch of the MZI is included in the radiation coupler so that the EMP scattering matrix will account for the detailed geometry of the sample. We also assume that only the EMP modes associated with the  $b(\omega)$  and  $b^\dagger(\omega)$  destruction and creation operators and the external radiation modes associated with the  $a(\omega)$  and  $a^\dagger(\omega)$  operators appear in the scattering matrix  $S(\omega)$ :

$$\begin{pmatrix} a_{\text{out}}(\omega) \\ b_{\text{out}}(\omega) \end{pmatrix} = \begin{pmatrix} S_{aa}(\omega) & S_{ab}(\omega) \\ S_{ba}(\omega) & S_{bb}(\omega) \end{pmatrix} \begin{pmatrix} a_{\text{in}}(\omega) \\ b_{\text{in}}(\omega) \end{pmatrix}. \quad (11)$$

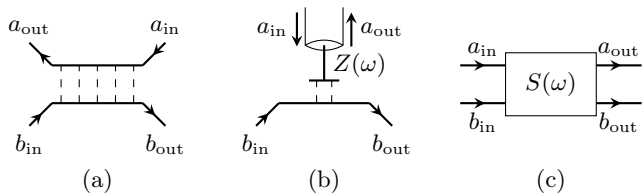


FIG. 4. (Color online) The edge-magnetoplasmon scattering approach describes many situations, such as for example (a) two counter-propagating edge channels capacitively coupled over a distance  $l$ , (b) a chiral edge channel capacitively coupled to a linear external circuit described by a frequency dependent impedance  $Z(\omega)$ . (c) Solving the equation of motions leads to a frequency dependent scattering matrix  $S(\omega)$  between the channel's edge-magnetoplasmon modes and the bosonic modes of the other system.

Depending on the design of the radiation coupler, the  $(a, a^\dagger)$  modes may be photonic (case of Fig. 4-(b)) or edge-magnetoplasmonic (see Fig. 4-(a)). These matrix elements are related to finite frequency admittances [47, 48, 59]. In principle, they could be inferred from experimental measurements [60]. Quantitative predictions can also be made from theoretical models of the radiation coupler. Experimentally relevant examples include the case of two counter-propagating edge channels (see Fig. 4-(a)) as well as the case of a capacitive coupling to a transmission line (see Fig. 4-(b)). Computations for the case of two counter-propagating edge channels in total mutual influence (see Fig. 4-(a)) are detailed in Appendix D. This specific radiation coupler model will be used all along the present manuscript to illustrate explicit examples.

#### B. The single electron radar equation

##### 1. Single particle scattering approach

We now derive the radar equation assuming that electronic propagation inside the radiation-coupler is described in terms of time dependent single particle scattering. We are neglecting electron-hole pairs creation by Coulomb interactions within the MZI. We also assume that the two QPCs are ideal electronic beam splitters with energy independent scattering matrix. Denoting by  $R(t, t')$  the amplitude for an electron to enter branch 1 at time  $t'$  and exit it at time  $t \geq t'$ , we can compute the Aharonov Bohm flux dependent contribution to the outgoing time dependent average electrical current  $\langle i_{1_{\text{out}}}(t) \rangle$ . In a MZI interferometer, its Aharonov-Bohm phase dependence reduces to

$$\langle i_{1_{\text{out}}}(t) \rangle = -e (I_0(t) + e^{i\phi_{AB}} I_+(t) + e^{-i\phi_{AB}} I_+(t)^*). \quad (12)$$

where  $\phi_{AB} = 2\pi\Phi_B/\Phi_0$  ( $\Phi_0 = h/e$  being the flux quantum). Denoting by  $\mathcal{A}(S \xrightarrow{j} 1_{\text{out}})$  the amplitude for an

electron to be emitted by the source S, propagating along branch  $j$  between the two QPCs and be detected in  $1_{\text{out}}$ , we have

$$I_+(t) = v_F \mathcal{A}(S \xrightarrow{1} 1_{\text{out}}) \mathcal{A}(S \xrightarrow{2} 1_{\text{out}})^* \quad (13)$$

with

$$\mathcal{A}(S \xrightarrow{1} 1_{\text{out}}) = \sqrt{T_A T_B} \int_{\mathbb{R}} R(t, t') \varphi_e(t') dt' \quad (14a)$$

$$\mathcal{A}(S \xrightarrow{2} 1_{\text{out}}) = -\sqrt{R_A R_B} \varphi_e(t - \tau_2). \quad (14b)$$

Note that, in the present context,  $2 \Re(I_+(t) e^{i\phi_{AB}})$  plays the role of  $\mathcal{P}_q$  in Sec. II. The quantity  $X_+(t)$  defined by  $I_+(t) = -\sqrt{R_A T_A R_B T_B} X_+(t)$  does not depend on the properties of the electronic beam splitters and completely determines the interference contribution to the average electrical current. It is equal to

$$X_+(t) = v_F \int_{\mathbb{R}} R(t, t') \varphi_e(t') \varphi_e(t - \tau_2)^* dt'. \quad (15)$$

This result is called the electronic radar equation by analogy with the existing signal processing literature [61]. Its integral over time

$$X_+^{(\text{dc})} = \int_{\mathbb{R}} X_+(t) dt. \quad (16)$$

represents the interference contribution to the total charge detected on the output 1 of the MZI. For a balanced MZI ( $T_A = T_B = 1/2$ ), the average dc current measured when the experiment is repeated at measurement frequency  $f_m$  is given by:

$$\langle i_{1_{\text{out}}}^{(\text{dc})} \rangle = -\frac{e f_m}{2} \left( 1 + \Re \left( e^{i\phi_{AB}} X_+^{(\text{dc})} \right) \right). \quad (17)$$

## 2. Coulomb interaction effects

The discussion of Sec. IIC suggests that the result in presence of Coulomb interactions and of an incoming quantum radiation is of the same form than Eq. (15) with an effective single electron scattering amplitude  $R_{\text{eff}}(t, t')$  that takes into account decoherence effects as well as the electron's back-action on the incoming quantum radiation. The formal derivation of this fact is given in Appendix E but, here, we will proceed along obtaining the form of the effective scattering amplitude using semi-qualitative arguments to emphasize its physical meaning.

In the absence of incoming electromagnetic radiation, the amplitude  $R_{\text{eff}}(t, t')$  is the amplitude for a single electron to propagate elastically across the branch 1, taking into account the capacitive coupling to the radiation coupler's radiation channel. Any process leading to the generation of an extra electron/hole pair within the edge channel or of an excitation within the electromagnetic environment would lead to decoherence in the MZI. This elastic scattering amplitude has already appeared

in studies of electronic decoherence in the MZI [62–65]. Electronic decoherence in MZI has been experimentally simulated using a voltage probe in Ref. [8], thereby showing the reduction of the interferometer's contrast by the amplitude (square root of the probability) for the electron to be transmitted across the probe.

In the absence of external radiation,  $R_{\text{eff}}(t, t')$  should then be the elastic scattering amplitude for an incoming single electron excitation injected at time  $t'$  in the presence of the Fermi sea to exit at time  $t$  without experiencing any inelastic scattering:  $R_{\text{eff}}(t, t') = \Theta(t-t') \mathcal{Z}_1(t-t')$  where

$$\mathcal{Z}_1(\tau) = \int_0^{+\infty} \tilde{\mathcal{Z}}_1(\omega) e^{-i\omega\tau} \frac{d\omega}{2\pi}. \quad (18)$$

is the Fourier transform of the elastic scattering amplitude  $\tilde{\mathcal{Z}}_1(\omega)$  for a single electron of energy  $\hbar\omega > 0$  across branch 1 of the MZI. This quantity, computed in Refs. [45, 58, 66], has recently been reconsidered in the light of recent experimental studies of electronic relaxation [9, 10, 67]. Going back to the discussion of Sec. IIC,  $\mathcal{Z}_1(\tau)$  corresponds to the product  $\mathcal{A}_1 \langle \Psi | \Psi' \rangle$  (Idle|Fizzled) when the radiation channel is fed with the vacuum state.

We now have to discuss the back-action of the electron in the presence of incoming radiation. The back action on the vacuum is already taken into account by the elastic scattering amplitude  $\mathcal{Z}_1(\tau)$  or  $\tilde{\mathcal{Z}}_1(\omega)$  but here, we consider the effect of the single electron current on the incoming photonic excitations.

An outgoing electron at time  $t$  corresponds, in terms of EMP, to a localized current pulse coming out of the branch 1. Such a current pulse comes from an incoming pulse in the edge channel 1 as well as some coherent pulse in the radiation channel whose amplitude can be inferred from the scattering matrix  $S(\omega)$ . Denoting by  $\Lambda_t(\omega) = -e^{i\omega t} / \sqrt{\omega}$  the corresponding amplitude of the mode  $b_{\text{out}}(\omega)$ , the amplitudes of the incoming pulses are given by:

$$\langle b_{\text{in}}(\omega) \rangle = S_{bb}^*(\omega) \Lambda_t(\omega) \quad (19a)$$

$$\langle a_{\text{in}}(\omega) \rangle = S_{ba}^*(\omega) \Lambda_t(\omega). \quad (19b)$$

Eq. (19b) gives the amplitude of the “back-action kick” on the incoming radiation associated with the detection of a electron localized at time  $t$  at the end of the upper MZI branch. Consequently, the unitary operator representing the back-action is the infinite dimensional displacement operator  $D_{a_{\text{in}}} [S_{ba}^* \Lambda_t]$  (see Eq. (B7) for its definition) associated with the back-action kick  $S_{ba}^* \Lambda_t$ .

The full back-action factor is then the average value of  $D_{a_{\text{in}}} [S_{ba}^* \Lambda_t]$  in the reduced density operator  $\rho_{\text{em}}$  describing the state of the incoming quantum radiation fed into the radiation coupler. But the contribution in the vacuum state  $|0\rangle$  for the  $a_{\text{in}}(\omega)$  modes is already included in  $\mathcal{Z}_1(t)$ . Consequently, the excess back-action on the incoming radiation is obtained by dividing  $\langle D_{a_{\text{in}}} [S_{ba}^* \Lambda_t] \rangle_{\rho_{\text{em}}}$  by  $\langle D_{a_{\text{in}}} [S_{ba}^* \Lambda_t] \rangle_{|0\rangle}$ . This leaves us

with the average value of the bosonic normal ordered back-action displacement operator for the prefactor representing the recoil of the incident radiation induced by a single electron excitation propagating across the upper branch of the MZI. We thus define the Franck-Condon factor

$$\mathcal{F}_{\rho_{\text{em}}}(t) = \left\langle : D_{a_{\text{in}}} [S_{ba}^* \Lambda_t] : \right\rangle_{\rho_{\text{em}}}. \quad (20)$$

by analogy with the Franck-Condon factor that appears in the spectroscopy of complex molecules [46] or in the Mössbauer effect [68, 69] where it is called the Lamb-Mössbauer factor. As noticed in Ref. [70] and explicitly derived here in Appendix F, the Franck-Condon factor contains information on the Full Counting Statistics of charge propagating within the radiation channel. More specifically, when the radiation channel is a chiral quantum Hall edge channel at  $\nu = 1$ ,

$$\mathcal{F}_{\rho}(t) = \left\langle : e^{2\pi i N(t)} : \right\rangle_{\rho_{\text{em}}}. \quad (21)$$

in which the  $N(t)$  operator represents a filtering of the charge operator flowing across the interaction region within the radiation channel.

The quantum interference contribution to the average outgoing electrical current then has the form

$$X_+(t) = v_F \int_{-\infty}^t R_{\text{eff}}(t, t') \varphi_e(t') \varphi_e(t - \tau_2)^* dt' \quad (22)$$

in which the effective single particle scattering amplitude is given by

$$R_{\text{eff}}(t, t') = \mathcal{Z}_1(t - t') \mathcal{F}_{\rho_{\text{em}}}(t). \quad (23)$$

In the case where independent repeated single electron experiments are performed, one can replace the product  $\varphi_e(t') \varphi_e(t - \tau_2)^*$  by the excess single electron coherence  $\Delta \mathcal{G}_S^{(e)}(t'|t - \tau_2)$  emitted by the imperfect single electron sources. This takes into account the statistical fluctuations in the imperfect emission of single electron excitations by the source  $S$ . Eq. (22) can then be interpreted as described on Fig. 5. Appendix G discusses the frequency domain form of the single electron radar equation and its interpretation.

Expression (23) takes into account electronic decoherence and the effect of the incoming quantum radiation. Together with the expressions for  $\mathcal{Z}_1(\tau)$  and for the Franck-Condon factor, Eqs. (22) and (23) form the central result of the single electron radar theory. The factorized form of the r.h.s. of Eq. (23) has an important consequence: the Franck-Condon factor appears as the ratio the time-resolved electron radar signal in the presence of the external radiation to the one in the absence of it:

$$\frac{[X_+(t)]_{\rho_{\text{em}}}}{[X_+(t)]_{|0}} = \mathcal{F}_{\rho_{\text{em}}}(t). \quad (24)$$

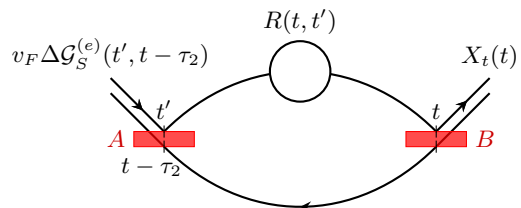


FIG. 5. Physical interpretation of the linear radar equation (22) in the time domain showing the contribution of incoming single electron coherence to the signal the temporal signal  $X_+(t)$ . The figure presents the product of two quantum amplitude: the one with an arrow oriented away from the source corresponds for a direct amplitude whereas the one, with the arrow arriving to the source corresponds to the complex conjugated amplitudes contributing to  $X_+(t)$ .

However, high precision time domain measurements of the average current with very large bandwidth are difficult to perform. We thus have to discuss how Eqs. (22) and (23) can be used to interpret the experimental data obtained by recording interference fringes on the dc average current which is the usual quantity measured with high precision.

### 3. The dc-current interference contrast

Assuming that the source could inject a very short electronic wave packet of duration  $\tau_e$  at time  $t_e$ , the electron radar signal in the presence of external radiation would (naively) be given by (see Appendix H)  $[X_+^{(\text{dc})}]_{\rho_{\text{em}}} \simeq \tau_e \mathcal{Z}(\tau_2) \mathcal{F}_{\rho_{\text{em}}}(t_e + \tau_2)$ . Comparing the result in the presence and in the absence of electronic radiation ( $\mathcal{F}_{|0}(t) = 1$ ) injected into the radiation channel then leads to

$$[X_+^{(\text{dc})}]_{\rho_{\text{em}}} \simeq [X_+^{(\text{dc})}]_{|0} \mathcal{F}_{\rho_{\text{em}}}(t_e + \tau_2). \quad (25)$$

Consequently, sweeping the emission time  $t_e$  of the infinitely short probe wave packet would sample  $\mathcal{F}_{\rho_{\text{em}}}(t_e + \tau_2)$  thereby providing us with a time resolved probe of the electromagnetic radiation. Note that the  $\tau_2$  time delay follows from ballistic propagation along the lower branch of the MZI. Unfortunately, Eq. (25) can only be seen as an heuristics since electronic wave packets with only positive energy components cannot be arbitrarily localized. Nevertheless, short duration Levitons [71] which are purely electronic provide us with a close analogue to a perfectly localized electronic excitation. But the issue of electronic decoherence must be addressed carefully.



## C. Leviton excitations

### 1. General result

As shown in Appendix I, the simple expression for the Leviton wave packet in the frequency domain enables us to derive a convenient form for  $X_+^{(\text{dc})}$  suitable for numerical evaluations:

$$X_+^{(\text{dc})} = \int_{\mathbb{R}} \tilde{\mathcal{F}}_{\rho_{\text{em}}}(\Omega) e^{-i\Omega(t_e + \tau_2)} f_{\tau_e, \tau_2}(\Omega) \frac{d\Omega}{2\pi} \quad (26)$$

in which  $\tilde{\mathcal{F}}_{\rho_{\text{em}}}(\Omega)$  denotes the Fourier transform of the Franck-Condon factor. The filter

$$f_{\tau_e, \tau_2}(\Omega) = 4\pi\tau_e \int_{|\Omega|/2}^{+\infty} \tilde{\mathcal{Z}}_1\left(\omega - \frac{\Omega}{2}\right) e^{-2\omega\tau_e} e^{-i(\omega - \frac{\Omega}{2})\tau_2} \frac{d\omega}{2\pi} \quad (27)$$

contains the effects of electronic decoherence along branch 1 and ballistic propagation along branch 2 of the interferometer for a Leviton excitation of duration  $\tau_e$ .

### 2. The vacuum baseline

Let us start by the dc contrast in the absence of external radiation ( $\rho_{\text{em}} = |0\rangle\langle 0|$ ) which we call the vacuum baseline:

$$\left[X_+^{(\text{dc})}\right]_{|0\rangle} = 4\pi\tau_e \int_0^{+\infty} \tilde{\mathcal{Z}}_1(\omega) e^{-2\omega\tau_e} e^{-i\omega\tau_2} \frac{d\omega}{2\pi}. \quad (28)$$

This quantity which represents the interference contrast, is reduced because of two different physical effects.

First of all, even in the absence of electronic decoherence, the asymmetry of times of flights along the target and the reference branch reduces the interference signal. For  $\tilde{\mathcal{Z}}_1(\omega) = e^{i\omega\tau_1}$  which corresponds to ballistic propagation along the target branch with time of flight  $\tau_1$ , we find

$$\left[X_+^{(\text{dc})}\right]_{|0\rangle} = \frac{2\tau_e}{2\tau_e + i\tau_{12}} \quad (29)$$

where  $\tau_{12} = \tau_1 - \tau_2$  characterizes the interferometer's imbalance. As expected, the interference signal decays as soon as  $|\tau_{12}|$  becomes larger than  $2\tau_e$ .

In the perspective of the electron radar, when using localized wavepackets in time such as the Levitons, one wishes to achieve such a time of flight synchronization to have the strongest information signal. Depending on the experimental situation, the geometry of the device may be constrained so that a lower bound  $\tau_e \gtrsim \min|\tau_{21}|/2 > 0$  is imposed, thereby intuitively limiting the time resolution of the interferometer. In other devices, we may be able to tune  $\tau_2$  in order to maximize the contrast in the absence of external situation. This is what we assume in the rest of this paper but the general expressions given by Eqs. (26) and (27) enable us to discuss any situation.

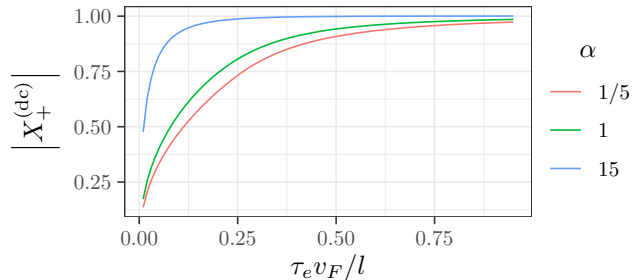


FIG. 6. (Color online) Contrast  $|X_+^{(\text{dc})}|$  of dc-current interference fringes for Leviton of duration  $\tau_e$  as function of  $\tau_e v_F / l$  in the absence of external radiation. The radiation coupler involves two counter-propagating edge channels in total mutual electrostatic influence over a distance  $l$  (see Appendix D). Curves have been plotted for  $\alpha = 1/5$  (red), 1 (green) and 15 (blue).

The second cause of interference contrast reduction is electronic decoherence. In the present formalism, electronic decoherence is associated with the decay of the electronic quasi-particle which is measured by the inelastic scattering probability  $\sigma_{\text{in}}(\omega) = 1 - |\tilde{\mathcal{Z}}_1(\omega)|^2$ .

Fig. 6 depicts  $\max_{\tau_2} |X_+^{(\text{dc})}|$  as a function of the Leviton's width  $\tau_e$ . as a function of  $v_F \tau_e / l$ . These graphs, obtained for a radiation coupler built from two counter-propagating edge channels in total electrostatic influence over a distance  $l$  via a geometric capacitance  $C_g$  (see Fig. 4-(a)), are plotted for different values of the dimensionless coupling constant

$$\alpha = \frac{e^2 l}{\hbar v_F C_g} \quad (30)$$

encoding the importance of Coulomb interaction effects within this radiation coupler (see Appendix D). As expected, at fixed  $\alpha$ , electronic decoherence is stronger for shorter Leviton pulses due to their high energy components. For a given  $\tau_e$ , it is also stronger at small  $\alpha$  compared to the Coulomb dominated regime (large  $\alpha$ ), an effect already predicted [72] and observed [73] when an electron of energy  $\hbar\omega_e$  propagates across a metallic island with Coulomb energy  $E_C \gg \hbar\omega_e$ . Finally, a 50 % contrast can be achieved when considering Levitons of durations  $\tau_e \gtrsim l/10 v_F$  which, in the case of  $l = 10 \mu\text{m}$  and  $v_F = 10^5 \text{ms}^{-1}$  corresponds to pulses of duration down to 10 ps.

### 3. Filtering of the Franck-Condon factor

We now consider the effect of the Leviton's duration as well as of electronic decoherence on the Franck-Condon prefactor. Without electronic decoherence, one expects the duration of the Leviton to be the limiting time resolution for accessing  $\mathcal{F}_{\rho_{\text{em}}}(t)$ . In the absence of electronic



decoherence, using  $\mathcal{Z}_1(\omega) = e^{i\omega\tau_1}$  leads to

$$\left[X_+^{(\text{dc})}\right]_{\rho_{\text{em}}} = \left[X_+^{(\text{dc})}\right]_{|0\rangle} (K_{\tau_e, \tau_{21}} \star \mathcal{F}_{\rho_{\text{em}}})(t_e + \tau_2) \quad (31)$$

where  $\left[X_+^{(\text{dc})}\right]_{|0\rangle}$  is given by Eq. (29) and the kernel

$$K_{\tau_e, \tau_{21}}(\tau) = \frac{1}{\pi} \frac{\tau_e + i\frac{\tau_{21}}{2}}{(\tau_e + i\frac{\tau_{21}}{2})^2 + (\tau - \frac{\tau_{21}}{2})^2} \quad (32)$$

encodes the way the Leviton's duration and the MZI's imbalance blur the temporal resolution on the Franck-Condon factor  $\mathcal{F}_{\rho_{\text{em}}}(t)$ . Eqs. (31) and (32) show that the duration  $\tau_e$  of the Leviton limits the time resolution for accessing  $\mathcal{F}_{\rho_{\text{em}}}(t)$ .

Electronic decoherence alters the expression of the kernel in Eq. (31). Let us now define  $\tau_1$  as the Wigner-Smith time delay associated with the elastic scattering amplitude  $\tilde{\mathcal{Z}}_1(\omega)$ :  $\tau_1 = -i[d(\ln(\tilde{\mathcal{Z}}_1(\omega)))/d\omega]$  at  $\omega = 0$ . We have to resort to the general filtering expressions given by Eqs. (26) and (27). As explained in Appendix I, the filtering function  $f_{\tau_e, \tau_2}(\Omega)$  always satisfies

$$f_{\tau_e, \tau_2}(\Omega \geq 0) = e^{-\Omega\tau_e} f_{\tau_e, \tau_2}(0). \quad (33)$$

which only requires the numerical computation of  $f_{\tau_e, \tau_2}(0)$ . But for  $\Omega < 0$ , one has

$$f_{\tau_e, \tau_2}(\Omega < 0) = e^{-|\Omega|\tau_e} e^{i\Omega\tau_{21}} \times 4\pi\tau_e \int_0^{+\infty} e^{-2\omega\tau_e} e^{-i\omega\tau_{21}} \tilde{\mathcal{Z}}_{1\star}(|\Omega| + \omega) \frac{d\omega}{2\pi}. \quad (34)$$

in which, for convenience, we have isolated the  $\tau_1$  dependence by introducing  $\tilde{\mathcal{Z}}_{1\star}(\omega) = e^{-i\omega\tau_1} \tilde{\mathcal{Z}}_1(\omega)$ . Its  $\Omega$  dependence is a priori more involved than in Eq. (33) and must be evaluated numerically.

Nevertheless, whenever the typical time scale associated with the radiation is much slower than  $\tau_e$  and  $\tau_D$ , defined as the inverse of the energy scale over which the inelastic scattering probability  $\sigma_{\text{in}}(\omega)$  starts to increase significantly, one may neglect the  $\Omega$ -dependence in  $\tilde{\mathcal{Z}}_{1\star}(|\Omega| + \omega)$ , thereby leading to

$$f_{\tau_e, \tau_2}(\Omega < 0) \simeq e^{-|\Omega|\tau_e} e^{-i|\Omega|\tau_{21}} f_{\tau_e, \tau_2}(0). \quad (35)$$

Eqs. (33) and (35) then lead to Eq. (31) with the same kernel  $K_{\tau_e, \tau_{21}}$  as in Eq. (32). Electronic decoherence is fully encapsulated in the vacuum baseline  $\left[X_+^{(\text{dc})}\right]_{|0\rangle}$ .

Eq. (35) is an ‘‘adiabatic radiation approximation’’ assuming that electronic decoherence can be neglected for the frequencies involved in the Franck-Condon factor. Note that this approximation does not assume that Leviton wavepackets, which involve much higher frequencies, experience a weak electronic decoherence. Electronic decoherence is indeed accounted for by the vacuum baseline contrast whose modulus can be much lower than the modulus of the r.h.s of Eq. (29) which is only valid for ballistic propagation along the target branch.

Interestingly, for very short Levitons and a balanced interferometer ( $\tau_{21} = 0$ ), the Kernel converges to the  $\delta(\tau)$  distribution and we recover the heuristic expression obtained in Eq. (25). The point is that we have an exact expression for the vacuum baseline given by Eq. (28). Moreover, we know that this is the result of an approximation which breaks down when electronic decoherence effects manifest themselves at frequencies similar to the inverse time scale of variation of  $\mathcal{F}_{\rho_{\text{em}}}(t)$ . More importantly, the results presented here enable us to go beyond this approximation and to consider an imbalanced ( $\tau_1 \neq \tau_2$ ) interferometer.

#### IV. PREDICTIONS FOR CLASSICAL AND QUANTUM RADIATION

We now consider various types of radiation directly relevant for forthcoming experiments. This includes classical radiation for which the physics of a time dependent phase seen by independent electrons of Sec. II B will be recovered in the voltage locked regime of the radiation coupler.

We then discuss the ability of the electron radar to probe non-classical radiation by considered squeezed states as well as single EMPs. Such quantum states of radiation cannot be described in terms of a classically fluctuating voltage and therefore, the full quantum approach of the previous section will be necessary to obtain quantitative predictions.

##### A. Classical radiation

We consider a classical drive  $V_g(t)$  applied to a top gate capacitively coupled to the edge channel along the target branch  $|x| \leq l/2$  of the MZI via a geometric capacitance  $C_g$  as depicted on Fig. 7. This corresponds to Fig. 4-b without dynamical degrees of freedom coupled to the top gate ( $Z(\omega) = 0$ ). This is the limit of an infinite number of electronic channels in the top gate's lead in Ref. [74].

Because there are no external dynamical degrees of freedom in this top gate model, its dynamics can be described by an input/output relations for the edge channel's EMP modes of the form:

$$i_{\text{out}}(\omega) = t(\omega) i_{\text{in}}(\omega) + Y(\omega) V_g(\omega) \quad (36)$$

where  $t(\omega)$  denotes the EMP transmission amplitude across the region  $|x| \leq l/2$  and the admittance  $Y(\omega)$  describes the response of the outgoing current to the top gate potential  $V_g(\omega)$ . Assuming total mutual influence between the top gate and target branch of the MZI,  $Y(\omega)$  is the finite frequency admittance of the electrical dipole formed by the top gate and the edge channel. It is related to  $t(\omega)$  by [45, 48, 59]:

$$Y(\omega) = \frac{e^2}{h} (1 - t(\omega)). \quad (37)$$

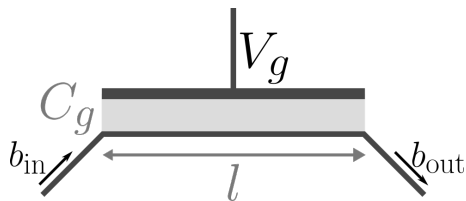


FIG. 7. A top gate is capacitively coupled to the  $|x| \leq l/2$  region of a chiral edge channel. It is driven by a time dependent gate voltage  $V_g(t)$ .  $C_g$  denotes the geometric capacitance between the two conductors.

Predictions for these coefficients can be obtained from the discrete element model corresponding to Fig. 7 presented in Appendix C.

Since the gate voltage translates the EMP operator  $b_{\text{in}}(\omega)$  by  $-Y(\omega)V_g(\omega)/e\sqrt{\omega}$ , it introduces a phase factor

$$\mathcal{F}_{V_g}(t) = e^{\frac{ie}{\hbar} \int_{\mathbb{R}} \Gamma(t-\tau)V_g(\tau) d\tau} \quad (38)$$

in front of the fermionic field coming out of the radiation coupler. The kernel  $\Gamma(\tau)$  is the inverse Fourier transform of  $-R_K Y(\omega)/i\omega$ . This shows that the effective single particle scattering amplitude retains the form given by Eq. (23) with  $\mathcal{Z}_1(\tau)$  given by Eq. (18) with  $t(\omega) = 1 - R_K Y(\omega)$  and  $\mathcal{F}_{V_g}(t)$  playing the role of  $\mathcal{F}_{\rho_{\text{em}}}(t)$  defined by (20) in the full quantum theory. In particular, because the only effect of the external drive  $V_g(t)$  is to introduce a phase, it does not contribute to electronic decoherence in the time domain.

The importance of Coulomb interactions within the  $|x| \leq l/2$  region depends on the dimensionless coupling constant  $\alpha = C_q/C_g$  defined by Eq. (30). For  $\alpha \ll 1$ , the voltage drop at the capacitance vanishes and therefore the electrons directly see the gate voltage  $V_g(t)$ . This is the voltage locked regime. On the other hand, for the  $\alpha \gtrsim 1$ , Coulomb interactions are so strong that they tend to block charge accumulation below the top gate. This is the Coulomb blocked regime.

### 1. The voltage locked regime

At very small  $\alpha$ , the electrochemical capacitance  $C_\mu = C_g C_q / (C_g + C_q) \simeq C_q$  is dominated by the quantum capacitance  $C_q \ll C_g$ . The voltage drop at the capacitance is negligible and electrons within the  $|x| \leq l/2$  region experience the gate potential  $V_g(t)$ . Moreover, in this limit  $t(\omega) \simeq e^{i\omega l/v_F}$ . Consequently, in this limit, the elastic scattering amplitude is  $\mathcal{Z}_1(\omega) \sim e^{i\omega l/v_F}$  and electronic decoherence can thus be neglected [45]. In other terms, there is no back-action of the incoming electron on the edge channel mediated by the top-gate which could lead to electronic decoherence. The effective scattering amplitude can be approximated by

$$R_{\text{eff}}(t, t') \simeq \delta\left(\tau - \frac{l}{v_F}\right) \mathcal{F}_{V_g}(t). \quad (39)$$

At very small  $\alpha$ ,  $\Gamma(\tau) = \mathbf{1}_{[0, l/v_F]}(\tau)$  and therefore, we recover Eq. (3) with  $\tau_1 = l/v_F$  and  $U(t) = V_g(t)$  as expected.

### 2. Intermediate regime

As  $\alpha$  is increased, electronic decoherence starts to appear but, as long as we keep the energy of the electronic excitation low enough, it can be neglected [45]. Nevertheless, increasing  $\alpha$  modifies the voltage seen by the electrons below the top gate which becomes a filtering of  $V_g(\omega)$  (see Eq. (C19)). Consequently, as long as electronic decoherence can be neglected, the MZI detects the accumulated electric phase associated with this filtered effective time dependent potential.

Nevertheless, for Leviton pulses, the discussion of Sec. III C shows that as long as the external voltage only involves low frequencies compared to the ones for which electronic decoherence starts to be significant, the adiabatic approximation of Eq. (35) can still be applied. The ratio of the contrast in the presence of  $V_g(t)$  and without can thus be obtained as

$$\frac{[X_+^{(\text{dc})}]_{V_g(t)}}{[X_+^{(\text{dc})}]_0} = \sum_{n \in \mathbb{Z}} \mathcal{F}_n[V_g(t)] e^{-2\pi n f \tau_e} \times e^{-2\pi i n f (t_e + \tau_2)} e^{-2\pi i n \Theta(-n) f \tau_{21}} \quad (40)$$

in which  $\mathcal{F}_n[V_g(t)]$  are the photo-assisted amplitudes associated with  $V_g(t)$  mediated through the top-gate, *id est* the Fourier coefficients of the Franck-Condon factor given by Eq. (38). Most importantly, the vacuum baseline  $[X_+^{(\text{dc})}]_0$  takes into account electronic decoherence effects.

Therefore, for an slow enough drive, even when electronic decoherence effects are strong, quantitative predictions for the relative dc contrast  $[X_+^{(\text{dc})}]_{V_g(t)}/[X_+^{(\text{dc})}]_0$  for Leviton pulses can still be obtained from the simple formalism discussed in Sec. II B, provided one properly takes into account the filtering of  $V_g(t)$  by the top gate.

### 3. The Coulomb blocked regime

The limit of large  $\alpha$  corresponds to the regime dominated by Coulomb interactions: they are so strong that no charge can accumulate on either on the  $|x| \leq l/2$  interaction region of the edge channel nor on the top gate. As explained in Appendix C 2, the outgoing EMP mode  $b_{\text{out}}(\omega)$  has a very small response to the external time dependent voltage. Consequently, the electron radar is weakly responding to the external voltage applied to the top gate. Consequently, this is not the proper regime of operation for the electron radar.

Note that electronic decoherence is not a problem in this regime. This echoes the results obtained recently in Ref. [75] in which a similar phenomenon occurs in a

MZI where the top gate in the strong coupling regime is replaced by a metallic island with small enough capacitance.

## B. Squeezed radiation

Let us now discuss the ability of the electron radar to detect squeezing by considering a Gaussian squeezed state.

### 1. General squeezing criterion

The key observation is that the radiation coupler is only sensitive to the radiation in a specific filtered mode. The Franck-Condon factor can then be computed using a Gaussian approximation for this mode. This leads to:

$$\mathcal{F}_{\rho_{\text{em}}}(t) = e^{i\phi(t)} e^{-\langle(\Delta Y_t)^2\rangle_{\rho_{\text{em}}} - \langle(\Delta Y_t)^2\rangle_{|0\rangle}}. \quad (41)$$

where the phase  $\phi(t)$  is due to the average value can be viewed as arising from the classical voltage felt by the electrons within the upper branch of the MZI. The other contribution comes from the Gaussian fluctuations of the quadrature

$$Y_t = \frac{i}{\sqrt{2}} \int_0^{\omega_c} \left( \frac{S_{ba}(\omega)}{\sqrt{\omega}} e^{-i\omega t} a_\omega - \text{h.c.} \right) d\omega \quad (42)$$

of the mode filtered by the radiation coupler. Here,  $\omega_c$  is any UV cutoff below which all the incoming radiation is emitted.

Because this second contribution changes  $|\mathcal{F}_{\rho_{\text{em}}}(t)|$ , it provides a sufficient criterion for squeezing: as soon as  $|\mathcal{F}_{\rho_{\text{em}}}(t)| > 1$  there is squeezing in the filtered mode since this is a signature of the fact that, for these values of  $t$ , fluctuations of the quadrature  $Y_t$  are smaller than in the vacuum state:  $\langle(\Delta Y_t)^2\rangle_{\rho_{\text{em}}} < \langle(\Delta Y_t)^2\rangle_{|0\rangle}$ .

### 2. Squeezing around a given frequency

Because of its relevance for experiments, let us discuss the ability of the electron radar to detect squeezed radiation in an electromagnetic mode around  $\omega \simeq \omega_0$  within a bandwidth  $\gamma_0$  such that  $Q_0 = \omega_0/\gamma_0$  is significantly larger than one so that  $S_{ba}(\omega)$  can be taken as constant for  $|\omega - \omega_0| \leq \gamma_0/2$ . In Appendix J we obtain show that for a time-periodic squeezed quantum noise whose power is concentrated in the narrow band  $|\omega - \omega_0| \leq \gamma_0/2$ , the Franck-Condon factor takes the form

$$\mathcal{F}_{\text{Sq}_z}(t) \simeq e^{\frac{|S_{ba}(\omega_0)|^2}{Q_0} \sinh(2|z|) [\cosh(2|z|) \cos(2\omega_0 t - \phi_0) - \sinh(2|z|)]} \quad (43)$$

where  $z$  is a squeezing parameter and  $\phi_0 = 2\text{Arg}(S_{ba}(\omega_0)) + \text{Arg}(z)$ . Its minimum value is

$$\min_t |\mathcal{F}_{\text{Sq}_z}(t)| = e^{-\frac{|S_{ba}(\omega_0)|^2}{2Q_0} (e^{4|z|} - 1)} < 1. \quad (44)$$

Let us recall that the compression factor for quadrature fluctuations for a squeezed mode in  $|\text{Sq}_z\rangle$  is given by  $e^{-4|z|}$ . As of today, a compression of 18% (0.86 dB) with respect to vacuum fluctuations has been achieved in quantum Hall edge channels [51]. Assuming a quality factor  $Q_0 = 5$  and no losses ( $|S_{ba}(\omega_0)|^2 = 1$ ) for the radiation coupler leads to a maximal increase of  $|\mathcal{F}_{\text{Sq}_z}(t)|$  by 1.8% whereas a 3 dB squeezing would lead to an increase by 5.1%.

### 3. Numerical results and discussion

Let us now discuss whether or not this is observable using Levitons. We have done it by evaluating numerically the filtering function  $f_{\tau_e, \tau_2}(\Omega)$  as well as the exact Fourier series of the Franck-Condon factor given by Eq. (43).

To have an intuition of the results, we have obtained analytical expressions within the adiabatic radiation approximation (Eq. (35)) by retaining only the first harmonics in the Fourier series of the Franck-Condon factor [76]. Using this approximation, an analytical expression for the maximum over  $t_e$  of the relative contrast with respect to the vacuum baseline as a function of  $|z|$  can be derived at the lowest order in  $\Lambda = |S_{ba}(\omega_0)|^2/Q_0$ :

$$\max_{t_e} \left| \frac{[X_+^{(\text{dc})}]_{\text{Sq}_z}}{[X_+^{(\text{dc})}]_{|0\rangle}} \right| \simeq 1 + \Lambda F_\eta(z) + \mathcal{O}(\Lambda^2) \quad (45)$$

where

$$F_\eta(z) = \eta \cosh(2|z|) \sinh(2|z|) - \sinh^2(2|z|) \quad (46)$$

with  $\eta = e^{-2\omega_0\tau_e} |\cos(2\omega_0\tau_2)| < 1$ . The behavior of  $F_\eta(z)$  governs the observability of squeezing as an increase of the interference contrast. It starts from 0 for  $z = 0$  and increases to a maximum positive value

$$\max_{|z|} \max_{t_e} \left| \frac{[X_+^{(\text{dc})}]_{\text{Sq}_z}}{[X_+^{(\text{dc})}]_{|0\rangle}} \right| \simeq 1 + \frac{\Lambda}{2} \left( 1 - \sqrt{1 - \eta^2} \right) + \mathcal{O}(\Lambda^2). \quad (47)$$

reached for  $|z|_{\text{opt}} = \text{arctanh}(\eta)/4$ . It is the maximum experimental signal expected for squeezing since  $F_\eta(z)$  decreases for  $|z| \geq |z|_{\text{opt}}$ . It becomes negative for  $|z| \geq 2|z|_{\text{opt}}$  meaning that, above  $2|z|_{\text{opt}}$ , the interference contrast for Levitons appears smaller than the vacuum baseline. This follows from the increase of the average photon number in  $|\text{Sq}_z\rangle$  with increasing  $z$ : as shown in Appendix J (see Eq. (J17)), randomly injected Levitons of width  $\tau_e$  will experience, on average, an increasing noise within the radiation coupler. For  $|z| \geq 2|z|_{\text{opt}}$ , this effect compensates the gain in contrast associated with sub-vacuum fluctuations experienced by the Leviton thereby leading to a decrease of the maximum relative contrast over  $t_e$  below unity.

Figure 8 displays the results of the numerical evaluation of the contrast in the voltage locked regime with 15 ps Levitons. Filled black lines correspond to the full numerical evaluation of the contrast. Dashed black horizontal lines correspond to the vacuum baseline  $|\langle X_+^{(\text{dc})} \rangle_{|0\rangle}|$ . Results are plotted for  $z \simeq 0.0496$  corresponding to 18 % (0.86 dB) noise reduction demonstrated in Ref. [51],  $z \simeq 0.0719$  corresponding to 1.25 dB (25 %) noise reduction and  $z \simeq 0.1733$  corresponding to 3 dB (50 %) noise reduction.

At some operating points, the contrast in the presence of the squeezed vacuum does exceed the vacuum baseline. It is a positive signature of squeezing but the overshoot is small: 0.3 % on a baseline of 57.5 %. The best numbers are obtained in the voltage locked regime for 1.25 dB squeezing and  $\omega_0 l / v_F = \pi$ . This frequency choice corresponds to the optimal coupling between the two edge channels. As expected from the analytics, increasing  $|z|$  too much leads to a decrease of the maximum relative relative contrast and even bring it below the vacuum baseline. Note also the good agreement between Eq. (45) and the numerical evaluation of the maximum absolute contrast. Note also that the best operating point ( $\omega_0 l / v_F = \pi$  and 1.25 dB squeezing) is close to the optimal maximum contrast given by Eq. (47). Shorter Levitons are expected to lead to a lower vacuum baseline (see Fig. 6) and also to shift the detrimental effect of the average noise towards higher values of  $|z|$ . This can be seen on Fig. 9 where 2.5 ps Levitons are considered, all other parameters being the same than for Fig. 8. We see that the maximum absolute contrast still increases with increasing  $|z|$  up to 3 dB squeezing instead of decreasing at 1.25 dB for 15 ps Levitons. Even if the absolute contrast overshoot over the vacuum baseline is not greater than for 15 ps Levitons, it comes over a 0.225 vacuum baseline instead of 0.57 and thus represents a two times increase in terms of the relative contrast increase. This clearly shows the pros and cons of shorter Leviton pulses: the filtering associated with their duration is better but they also lead to a lower vacuum baseline.

### C. Fock states

We now consider the problem of detecting Fock states in a specific EMP mode. This state being non-Gaussian, the Gaussian result given by Eq. (41) breaks down.

#### 1. The Franck-Condon factor

We consider  $|N; \chi\rangle$ , the  $N$  photon Fock state in the normalized mode  $\chi$ . An explicit computation detailed in Appendix B2 shows that the Franck-Condon factor  $\mathcal{F}_{|N; \chi\rangle}(t)$  is then given by

$$\mathcal{F}_{|N; \chi\rangle}(t) = L_N \left( 2\pi |\langle \chi | S_{ba}^* \Lambda_t \rangle|^2 \right) \quad (48)$$

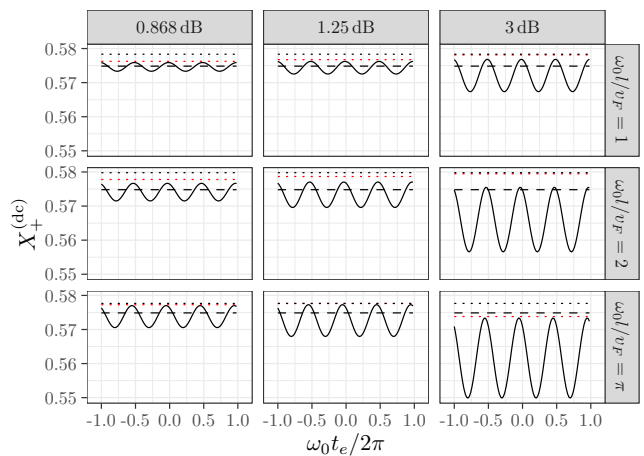


FIG. 8. The various plots depict the interference contrast  $\left[ X_+^{(\text{dc})} \right]_{\text{Sq}(z)}$  for Leviton excitations of width  $\tau_e = 15$  ps assuming a  $10 \mu\text{m}$  long radiation coupler with  $v_F = 10^5 \text{ m s}^{-1}$  with coupling strength  $\alpha = 1/5$ . The plots show the absolute contrast as a function of the dimensionless injection time  $v_F t_e / l$  for different values of the squeezing (expressed in dB) and  $\omega_0 l / v_F = 1, 2$  and  $\pi$ . The dashed black horizontal lines correspond to the vacuum baseline  $\left[ X_+^{(\text{dc})} \right]_{|0\rangle}$ . The dotted black lines correspond to the maximally optimized maximum contrast given by Eq. (47) whereas the dotted red lines correspond to the evaluation of Eq. (45) for the actual value of the squeezing parameter considered in the example.

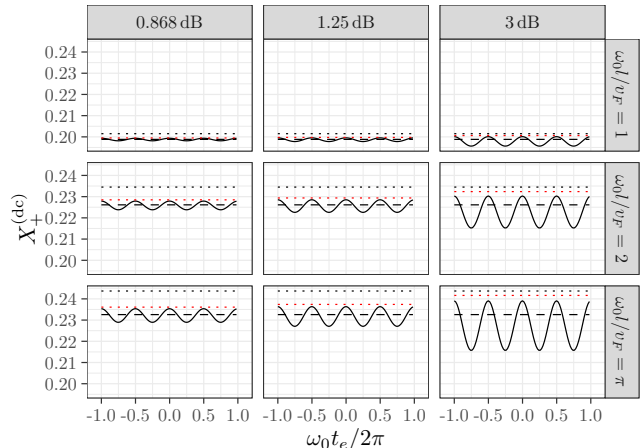


FIG. 9. The various plots depict the interference contrast  $\left[ X_+^{(\text{dc})} \right]_{\text{Sq}(z)}$  for Leviton excitations of width  $\tau_e = 2.5$  ps assuming the same parameters and legend than in Fig. 8.

in which  $L_N$  denotes the  $N$ -th Laguerre polynomial and

$$\langle S_{ba}^* \Lambda_t | \chi \rangle = - \int_0^{+\infty} \frac{S_{ba}(\omega)}{\sqrt{\omega}} e^{-i\omega t} \chi(\omega) \frac{d\omega}{2\pi}. \quad (49)$$

We now focus on the specific example of an EMP mode whose wavefunction in the frequency domain  $\chi(\omega)$  is centered at  $\omega_0$  with Lorentzian lineshape of width  $\gamma_0$ . We

assume that  $\omega_0/\gamma_0$  is significantly larger than unity, as expected from spontaneous emission by a two level emitter.

### 2. Narrow bandwidth approximation

Denoting by  $x(t) = 2\pi |\langle \chi | S_{ba}^* \Lambda_t \rangle|^2$  the argument of the Laguerre polynomial in Eq. (48), and assuming that  $\chi(\omega)$  is concentrated around  $\omega_0$  with a small bandwidth  $\gamma_0 \ll \omega_0$ ,  $x(t)$  can be rewritten as (see Appendix K):

$$x(t) \simeq 2\pi \frac{\gamma_0}{\omega_0} |S_{ba}(\omega_0)|^2 \frac{\langle \mathcal{J}_Q(t) \rangle_{|1;\chi\rangle}}{\gamma_0 \hbar \omega_0}. \quad (50)$$

in which

$$\mathcal{J}_Q(t) = \frac{R_K}{2} : i(t)^2 : . \quad (51)$$

denotes the instantaneous heat current operator injected in the radiation channel expressed in terms of the electrical current  $i(t)$ . Consequently, for  $\gamma_0/\omega_0 \lesssim 1$ , the expansion  $L_N(x) \simeq 1 - Nx + \mathcal{O}(x^2)$  for the Laguerre polynomial leads to:

$$\mathcal{F}_{|N;\chi\rangle}(t) \simeq 1 - 2\pi N \frac{\omega_0}{\gamma_0} |S_{ba}(\omega_0)|^2 \frac{\langle \mathcal{J}_Q(t) \rangle_{|1;\chi\rangle}}{\gamma_0 \hbar \omega_0}. \quad (52)$$

Therefore, within this approximation[77], the Franck-Condon factor provides a direct measurement of the average heat current carried by the single EMP. Provided  $2\pi N \omega_0 |S_{ba}(\omega_0)|^2 / \gamma_0$  does not take large values for the values of  $N$  with non negligible  $p_N$  and noticing that  $\langle \mathcal{J}_Q(t) \rangle_{|N;\chi\rangle} = N \langle \mathcal{J}_Q(t) \rangle_{|1;\chi\rangle}$  enables us to average over  $N$  and show that

$$\mathcal{F}_{\rho_{\text{mix}}}(t) \simeq 1 - 2\pi \frac{\omega_0}{\gamma_0} |S_{ba}(\omega_0)|^2 \frac{\langle \mathcal{J}_Q(t) \rangle_{\rho_{\text{mix}}}}{\gamma_0 \hbar \omega_0}. \quad (53)$$

for  $\rho_{\text{mix}} = \sum_{N=0}^{+\infty} p_N |N;\chi\rangle \langle N;\chi|$ . For such radiation, the electron radar acts as a time resolved ‘‘quantum bolometer’’ by converting the incident energy flux within the radiation channel into the Franck-Condon factor. As before, assessing the potential for single EMP detection requires discussing experimentally realistic signals in experimentally realistic situations.

### 3. Results and discussion

We consider lorentzian EMP modes of duration  $\gamma_0^{-1} = 1 \text{ ns} = 10l/v_F$  centered on  $\omega_0$  such that  $\omega_0 l/v_F = 2, 5.5$  and 10 corresponding to respective frequencies 3.2 GHz, 8.75 GHz and 15.9 GHz. Levitons of duration  $\tau_e = 10 \text{ ps}$  have a time resolution of the order of 1 % of the EMP wave packet duration.

Figure 10 depicts the various numerical estimates for the relative contrast decrease on the dc average current in the presence of the single EMP with respect to the

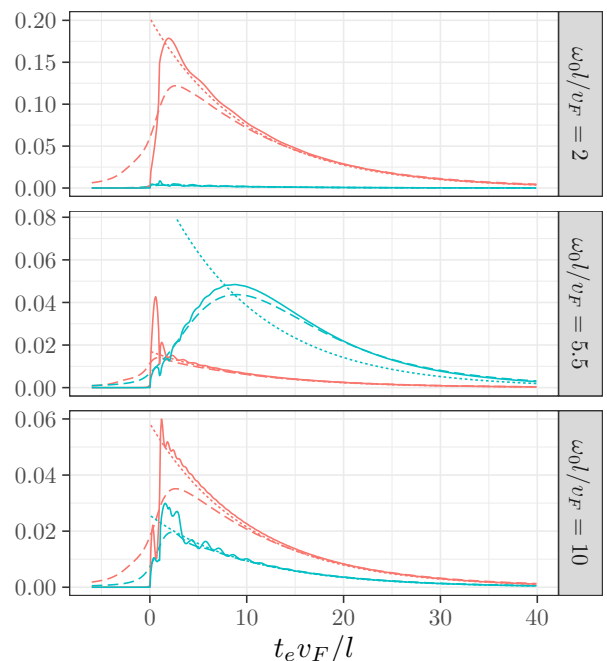


FIG. 10. (Color online) Plot of the relative contrast decrease  $1 - \left| \frac{[X_+^{(\text{dc})}]_{|1;\chi\rangle}}{[X_+^{(\text{dc})}]_{|0\rangle}} \right|$  (dashed line) associated with the detection of a single EMP with energy  $\hbar\omega_0$  and Lorentzian lineshape of width  $\gamma_0 = 10^9 \text{ s}^{-1}$  when using Leviton pulses of width  $\tau_e = 10 \text{ ps}$  injected at times  $t_e$ . The radiation coupler is described in Appendix D. Red curves correspond to the voltage locked regime ( $\alpha = 1/10$ ) whereas the blue curves correspond to the Coulomb blocked regime ( $\alpha = 15$ ). Three different values of  $\omega_0 l/v_F$  have been considered. The dotted line corresponds to  $1 - \mathcal{F}_{|1;\chi\rangle}(t)$  using the analytic expression given by Eq. (52) whereas the full line represents  $x(t) = 2\pi |\langle \chi | S_{ba} \Lambda_t \rangle|^2$ .

vacuum baseline. With the parameters considered here, the latter contrast is expected to be above 50 % (see Sec. III B 3). The results, presented on Fig. 10, confirm that an observable relative contrast decrease of a few % can be expected. The dominant effect in the amplitude of the effect comes from the transparency of the radiation coupler in the bandwidth of the incident radiation.

The precise comparison with numerical evaluations shows that the analytical result given by Eq. (50) is semi-quantitatively recovered except on short time scales where higher frequency contributions are expected to matter. It also departs from the numerical evaluation of  $x(t)$  because of the filtering of high frequencies associated with the finite duration of the Leviton.

## V. CONCLUSIONS AND PERSPECTIVES

In this work, we have discussed single electron interferometric sensing of classical and quantum electromagnetic fields. The idea is to probe a time dependent, possibly

quantum, electromagnetic field by coupling it to one of the branches of an electronic MZI fed by single electron excitations which provides a very sensitive although minimally invasive probe. Information about the field is then obtained by measuring the interference contribution to the average outgoing dc current from the interferometer.

We have developed a general framework describing such a single electron interferometer in the Aharonov-Bohm regime for any type of “radiation coupler” realizing the capacitive coupling between the radiation to be probed and the electrons propagating within the MZI. In the limit where the radiation coupler is strongly dominated by its quantum capacitance, the electrons directly experience the voltage imposed by the external radiation. A coherent state of the incoming radiation just imprints a time-dependent phase on the single electron excitations injected into the MZI, as expected when Coulomb interaction effects between electrons can be neglected. However, our framework goes beyond this simple picture of time dependent single particle scattering and fully incorporates electronic decoherence effects associated with Coulomb interactions. Although our formalism enables discussing any single electron excitations, we have for simplicity focused on Leviton pulses which, when sufficiently short, can be used to sample the external radiation when sweeping their injection time.

Besides the case of a classical drive, we have explored the potential for sensing quantum features of the probed radiation by considering two examples of quantum radiation. First, for Gaussian states for the incident radiation, an operational criterion for squeezing detection via short duration wave packets is given. Realistic estimates suggest that a 1.15 dB squeezing within a nearby quantum Hall edge channel could, in principle, lead to an observable increase of the contrast of Aharonov-Bohm interference fringes compared to the vacuum baseline when using 15 ps Levitons. Secondly, we have shown that a single EMP propagating in the radiation edge channel could be detected via the transient interference contrast decrease induced by its quantum noise. Moreover, we have seen that, as a function of their injection time, the interference contrast for short enough Levitons semi-quantitatively images the average instantaneous heat current carried by the single edge-magnetoplasmon.

These two examples suggest that the single electron interferometer fed by suitably short Levitons may be used as a time resolved quantum noise sensor on subnanosecond, possibly down to few picoseconds, time scales.

Several perspectives are opened by the present work. First of all, obtaining more quantitative predictions for forthcoming experiments may require completing the present study to account for finite temperature and charging effects as in Refs. [78–80]. Secondly, recent progresses in the shaping [74] and characterization [12, 38] of electronic excitations emitted by single electron sources [81] suggest investigating the potential of well known techniques from classical radar engineering to improve

our ability to probe very short dynamical time scales of the incident electromagnetic radiation [82]. An important related question is to design a set of single electron excitations enabling a full reconstruction of the effective single-particle amplitude induced by the coupling to the external radiation, thereby mimicking the use of infinite chirps [83] in radars and sonars to reconstruct the target’s scattering amplitude by inverse Radon transform, a technique commonly used in computed tomography scans [84], quantum optics [85, 86] and for reconstructing the quantum state of solitary electrons [37]. However, in the presence of a Fermi sea, infinite chirps cannot be generated because of the Fermi sea, thereby leaving the problem of tomographic reconstruction of the effective single electron scattering amplitude open for further investigation.

Another important issue consists in studying the signal to noise ratio in such an electronic interferometer. Quantitative predictions for the current noise would open the way to discussing the basic question of quantum metrology in the present context: how to choose the source and the measured quantity in order to discriminate between various quantum states of the incoming radiation in an optimal way. This is analogous to the problem of super-resolution encountered in optics and astronomy [87–90]. The standard methods used in this field can certainly be transposed but this requires an evaluation of the outgoing current noise. Motivated by the recent work [91], one could also investigate whether or not injecting few electron states into the MZI would lead to some quantum advantage as entangled states do in quantum metrology [92].

Finally, the present work discusses the information extracted from repeated experiments in which a precise synchronization between the source and the external radiation can be established. The potential emergence of one-shot single electron detection [15, 93, 94] calls for an adaptation of the present work to these forthcoming detection methods. These very interesting questions, which go well beyond the scope of the present work, are left for future investigations.

## ACKNOWLEDGMENTS

This work was supported by the ANR grant “QuSig4QuSense” (ANR-21-CE47-0012) and by the Joint Research Project “SEQUOIA” (17FUN04) within the European Metrology Programme for Innovation and Research (EMPIR) co-financed by the Participating States and from the European Union’s Horizon 2020 research and innovation programme. P. D. acknowledges funding by the Latvian Quantum Initiative during his stay at University of Latvia in Riga. We warmly thank C. Bauerle, A. Feller, D. Ferraro, V. Kashcheyevs, for useful discussions as well as C. Altimiras and C. Flindt for pointing out relevant references.

## Appendix A: Notations and normalizations

This appendix recalls the basic conventions used for fermionic modes and electronic single particle states within the present work.

### 1. Electronic modes and wave packets

The mode decomposition for fermionic fields is defined by

$$\psi(t) = \int_{\mathbb{R}} c(\omega) e^{-i\omega t} \frac{d\omega}{\sqrt{2\pi v_F}} \quad (\text{A1})$$

so that these modes obey the canonical anticommutation relations

$$\{c(\omega), c^\dagger(\omega')\} = \delta(\omega - \omega'). \quad (\text{A2})$$

Equivalently, we have

$$c(\omega) = \sqrt{\frac{v_F}{2\pi}} \int_{\mathbb{R}} \psi(t) e^{i\omega t} dt. \quad (\text{A3})$$

Given an electronic wave packet described by a normalized wave function  $\varphi_e(x)$  such that

$$\int_{\mathbb{R}} |\varphi_e(x)|^2 dx = 1 \quad (\text{A4})$$

Throughout this paper, we will use the notation  $\varphi_e(t)$  for  $\varphi_e(-v_F t)$  so that

$$v_F \int_{\mathbb{R}} |\varphi_e(t)|^2 dt = 1. \quad (\text{A5})$$

We define

$$\tilde{\varphi}_e(\omega) = v_F \int_{\mathbb{R}} \varphi_e(t) e^{i\omega t} dt \quad (\text{A6})$$

so that

$$\frac{1}{v_F} \int_{\mathbb{R}} |\tilde{\varphi}_e(\omega)|^2 \frac{d\omega}{2\pi} = 1. \quad (\text{A7})$$

The creation operator for the electronic wave packet  $\varphi_e$  is then defined as

$$\psi^\dagger[\varphi_e] = v_F \int_{\mathbb{R}} \varphi_e(t) \psi^\dagger(t) dt \quad (\text{A8a})$$

$$= \int_{\mathbb{R}} \tilde{\varphi}_e(\omega) c^\dagger(\omega) \frac{d\omega}{\sqrt{2\pi v_F}} \quad (\text{A8b})$$

## Appendix B: Bosonization and bosonic modes

Here, we briefly recall useful formulae in the bosonization of quantum Hall edge channels as well as for dealing with bosonic excitations.

### 1. Bosonization of a quantum Hall edge channel

For a right moving quantum Hall edge channel at filling fraction  $\nu = 1$ , the charge and current densities are related to the free chiral right moving field  $\phi_R(x, t)$  by

$$\rho_R(x, t) = -\frac{e}{\sqrt{\pi}} (\partial_x \phi_R)(x, t) \quad (\text{B1a})$$

$$i_R(x, t) = \frac{e}{\sqrt{\pi}} (\partial_t \phi_R)(x, t) \quad (\text{B1b})$$

and the right moving field is decomposed in terms of bosonic destruction and creation operators  $b(\omega)$  and  $b^\dagger(\omega)$  for  $\omega > 0$  satisfying

$$[b(\omega), b^\dagger(\omega')] = \delta(\omega - \omega') \quad (\text{B2})$$

by

$$\phi_R(x, t) = \frac{-i}{\sqrt{4\pi}} \int_{\mathbb{R}^+} \left( b(\omega) e^{i\omega(x/v_F - t)} - \text{h.c.} \right) \frac{d\omega}{\sqrt{\omega}} \quad (\text{B3})$$

This leads to the following mode decompositions for the charge and current densities

$$\rho_R(x, t) = -e \int_{\mathbb{R}^+} \sqrt{\omega} \left( b(\omega) e^{i\omega x/v} + b^\dagger(\omega) e^{-i\omega x/v} \right) \frac{d\omega}{2\pi v} \quad (\text{B4a})$$

$$i_R(x, t) = -\frac{e}{2\pi} \int_{\mathbb{R}^+} \sqrt{\omega} \left( b(\omega) e^{i\omega x/v} - b^\dagger(\omega) e^{-i\omega x/v} \right) d\omega. \quad (\text{B4b})$$

thereby connecting the finite frequency current to the EMP creation and destruction operators:  $i_R(\omega > 0) = -e\sqrt{\omega} b(\omega)$ .

The right moving electronic field is then expressed in terms of the chiral bosonic field by

$$\psi_R(x, t) = \frac{\hat{U}}{\sqrt{2\pi a}} e^{i\sqrt{4\pi} \phi_R(x, t)} \quad (\text{B5})$$

in which  $a$ , which has the dimension of a length, is an UV cut-off and  $\hat{U}$  is the operator lowering the total fermion number in the edge channel. Using the mode expansion (B3), one arrives at the expression for  $\psi_R(x = 0, t)$  in terms of an infinite dimensional displacement operator:

$$\psi_R(0, t) = \frac{\hat{U}}{\sqrt{2\pi a}} D_b[\Lambda_t] \quad (\text{B6})$$

in which  $\Lambda_t(\omega) = -e^{i\omega t}/\sqrt{\omega}$ . The infinite dimensional displacement operator with complex valued functional parameter  $\Lambda : \omega \mapsto \Lambda(\omega)$  is defined as:

$$D_b[\Lambda] = \exp \left[ \int_0^{+\infty} (\Lambda(\omega) b^\dagger(\omega) - \text{h.c.}) d\omega \right]. \quad (\text{B7})$$



## 2. Conventions for bosonic excitations

A normalized excitation is described by  $\chi(\omega)$  for  $\omega > 0$  such that

$$\int_0^{+\infty} |\chi(\omega)|^2 \frac{d\omega}{2\pi} = 1 \quad (\text{B8})$$

so that the single particle state

$$|\chi\rangle = \int_0^{+\infty} \chi(\omega) b^\dagger(\omega) |\emptyset\rangle \frac{d\omega}{\sqrt{2\pi}} \quad (\text{B9})$$

is normalized. If we define the corresponding creation operator

$$b^\dagger[\chi] = \int_0^{+\infty} \chi(\omega) b^\dagger(\omega) \frac{d\omega}{\sqrt{2\pi}} \quad (\text{B10})$$

and its adjoint  $b[\chi]$ , these operators obey the commutation relations

$$[b[\chi_1], b^\dagger[\chi_2]] = \langle \chi_1 | \chi_2 \rangle \mathbf{1} \quad (\text{B11})$$

where  $\langle \chi_1 | \chi_2 \rangle$  denotes the scalar product

$$\langle \chi_1 | \chi_2 \rangle = \int_0^{+\infty} \chi_1(\omega)^* \chi_2(\omega) \frac{d\omega}{2\pi}. \quad (\text{B12})$$

on the space  $\mathcal{L}_2(\mathbb{R}^+)$  of square-summable functions on  $\mathbb{R}^+$ . Note that with these conventions  $\chi(\omega) = \sqrt{2\pi} \langle \omega | \chi \rangle$  where  $|\omega\rangle = b^\dagger(\omega) |\emptyset\rangle$  is the single photon state resolved in energy.

Finally, when given an orthonormal basis of normalized single particle states  $|\chi_n\rangle$  indexed by  $n$ , the mode operators  $b(\omega)$  can be expressed in terms of the  $b_n = b[\chi_n]$  as

$$b(\omega) = \frac{1}{\sqrt{2\pi}} \sum_n \chi_n(\omega) b_n. \quad (\text{B13})$$

Starting from a normalized single particle state  $|\chi\rangle$ , we can express  $b^\dagger(\omega)$  in terms of  $b^\dagger[\chi]$  and of  $b^\dagger[\chi_\perp]$  where  $|\chi_\perp\rangle$  denotes the normalized projection of  $|\omega\rangle$  on the space of single particle excitations orthogonal to  $|\chi\rangle$ :

$$b^\dagger(\omega) = \langle \chi | \omega \rangle b^\dagger[\chi] + \sqrt{1 - |\langle \chi | \omega \rangle|^2} b^\dagger[\chi_\perp]. \quad (\text{B14})$$

## Appendix C: The classically driven edge channel

In this appendix, we discuss two models for a classically driven edge channel. In the first model discussed in Sec. C 1, we consider that a classical drive  $U(t)$  is directly applied to the electrons propagating within the edge channel. However, in experiments, the external drive is not directly applied to the edge channels but to a top gate. This leads us to the second model discussed in Sec. C 2 which involves a capacitive coupling between a finite length region of the edge channel and a top gate to which the time-dependent classical voltage is applied. We then discuss how this second model reduces to the first one in the regime of weak Coulomb interactions.

## 1. Direct coupling to the external voltage

Let us first consider electrons propagating within a chiral edge channel with Fermi velocity  $v_F$  and experiencing in the  $0 \leq x \leq l$  a time dependent  $U(x, t)$ .

### a. EMP scattering

The starting point is the equation of motion for the chiral bosonic field  $\phi_R(x, t)$  built from the EMP modes of the chiral edge channel:

$$(\partial_t + v_F \partial_x) \phi_R(x, t) = \frac{e\sqrt{\pi}}{h} U(x, t) \quad (\text{C1})$$

This equation can be solved using the method of characteristics:

$$\begin{aligned} \phi_R(x + v_F \tau, t + \tau) &= \phi_R(x, t) \\ &+ \frac{e\sqrt{\pi}}{h} \int_0^\tau U(x + v_F \tau', t + \tau') d\tau' \end{aligned} \quad (\text{C2})$$

which gives the outgoing field  $\phi_{R,\text{out}}(t) = \phi_R(l, t)$  in terms of the incoming field  $\phi_{R,\text{in}}(t) = \phi_R(0, t)$  and of the time and space dependent potential  $U(x, t)$ :

$$\begin{aligned} \phi_{R,\text{out}}(t) &= \phi_{R,\text{in}}(t - l/v_F) \\ &+ \frac{e\sqrt{\pi}}{h} \int_0^{l/v_F} U(v_F \tau', t + \tau' - l/v_F) d\tau'. \end{aligned} \quad (\text{C3})$$

The field and therefore the EMP modes propagate ballistically at velocity  $v_F$  and the time and space dependent voltage adds a source term.

For comparison with subsequent models, let us consider the case where  $U(x, t)$  is uniform within the  $|x| \leq l/2$  region and equal to the time-dependent potential  $U(t)$  and compute how the  $b(\omega)$  EMP annihilation operator is scattered. Specializing Eq. (C3), re-expressing it in the Fourier domain and using the  $b(\omega)$  operators leads to:

$$b_{\text{out}}(\omega) = e^{i\omega\tau_l} b_{\text{in}}(\omega) + \frac{iel\sqrt{\omega}}{hv_F} f\left(\frac{\omega l}{v_F}\right) U(\omega). \quad (\text{C4})$$

where  $\tau_l = l/v_F$  is the electronic time of flight across the region of length  $l$  to which the potential is applied and  $f(X) = (e^{iX} - 1)/iX$ . Rewriting this scattering formula in terms of incoming and outgoing currents leads to

$$i_{\text{out}}(\omega) = e^{i\omega\tau_l} i_{\text{in}}(\omega) - i\omega C_q(\omega) U(\omega) \quad (\text{C5})$$

in which we recognize the  $\omega$ -dependent dynamical quantum capacitance

$$C_q(\omega) = \frac{e^2 l}{hv_F} f\left(\frac{\omega l}{v_F}\right) \quad (\text{C6})$$

which, in the present case, reduces to the expected  $C_q = e^2 l / hv_F$  at low frequencies.

### b. Electronic phase

Eq. (C3) can then be used to compute how the electronic field is propagated using Eq. (B6):

$$\psi_{\text{out}}(t) = e^{i\vartheta_U(t)} \psi_{\text{in}}(t - l/v_F) \quad (\text{C7a})$$

$$\vartheta_U(t) = \frac{e}{\hbar} \int_0^{l/v_F} U(v_F \tau', t + \tau' - l/v_F) d\tau' \quad (\text{C7b})$$

This corresponds to a time dependent single particle scattering matrix for the electrons:

$$S(t, t') = \delta(t - t' - l/v_F) e^{i\vartheta_U(t)} \quad (\text{C8})$$

which precisely described the propagation at constant velocity  $v_F$  of a particle of charge  $-e$ , traveling across the region where the potential  $U(x, t)$  is present between space-time coordinates  $(0, t - l/v_F)$  and  $(l, t)$ . For such a particle, the accumulated phase  $\vartheta_U(t)$  is the potential seen along a trajectory that connects  $(0, t - l/v_F)$  to  $(l, t)$ .

## 2. The classically driven top gate

### a. EMP scattering

We now consider a top gate classically driven by a time dependent voltage  $V_g(t)$  and capacitively coupled to a chiral edge channel. This region is modeled as a capacitor with geometric capacitance  $C_g$  involving the top gate and part of a chiral edge channel of length  $l$  (see Fig. 7) in a discrete element description. The two conductors are in total influence. We want to get the expression of the outgoing EMPs modes  $b_{\text{out}}$  in terms of the incoming ones  $b_{\text{in}}$  and of  $V_g$ .

The basic equations for this system are the equation of motion for the chiral bosonic field  $\phi_R(x, t)$ , field built from the EMP modes of the chiral edge channel:

$$(\partial_t + v_F \partial_x) \phi_R(x, t) = \frac{e\sqrt{\pi}}{\hbar} U(x, t) \quad (\text{C9})$$

$U(x, t)$  is the potential seen by the electrons. If we assume that  $U(x, t)$  is uniform in the  $|x| \leq l/2$  region, it can be calculated by adding the potential drop across the capacitor to  $V_g(t)$ :

$$U(t) - V_g(t) = \frac{Q(t)}{C_g} \quad (\text{C10})$$

where  $Q(t)$  denotes the excess charge in the  $|x| \leq l/2$  of the chiral edge channel. Using the bosonization expression

$$Q(t) = \frac{e}{\sqrt{\pi}} (\phi_R(-l/2, t) - \phi_R(l/2, t)) \quad (\text{C11})$$

in addition of Eqs. (C9) and (C10), we can obtain a closed differential equation for  $\phi_R(x, t)$  within the  $|x| \leq l/2$  region. This method is identical to the one used to discuss

the Coulomb interaction effects within a chiral edge channel in Ref. [45].

The final result can be expressed as connecting the outgoing EMP modes  $b_{\text{out}}(\omega)$  to the incoming EMP modes  $b_{\text{in}}(\omega)$  and  $V_G(\omega)$ . This relation is best expressed in terms of the incoming and outgoing currents using  $i(\omega) = -e\sqrt{\omega} b(\omega)$ :

$$i_{\text{out}}(\omega) = t(\omega) i_{\text{in}}(\omega) + \frac{e^2}{\hbar} (1 - t(\omega)) V_G(\omega). \quad (\text{C12})$$

in which, using  $X = \omega l/v_F$ :

$$t(\omega) = e^{iX} \frac{1 + \alpha f^*(X)}{1 + \alpha f(X)} \quad (\text{C13})$$

where as before  $f(X) = (e^{iX} - 1)/iX$  and

$$\alpha = \frac{e^2 l}{\hbar v_F C_g} \quad (\text{C14})$$

a dimensionless coupling constant whose physical meaning is discussed in Sec. III C.

### b. Impedance & discussion

Folding the edge channel as shown on Fig. 11-a enables us to consider the quantum  $RC$  circuit formed by the top gate and the folded edge channel. Because of the total mutual influence, its admittance matrix defined by

$$\mathbf{Y}_{\alpha, \beta}(\omega) = \frac{\partial \langle i_{\alpha}(\omega) \rangle}{\partial V_{\beta}(\omega)} \quad (\text{C15})$$

where  $(\alpha, \beta) \in \{u, d\}^2$  is both gauge invariant and charge conserving [95] and therefore determined by a single finite frequency admittance

$$\mathbf{Y}(\omega) = Y(\omega) \begin{pmatrix} 1 & -1 \\ -1 & 1 \end{pmatrix} \quad (\text{C16})$$

with

$$Y(\omega) = \frac{e^2}{\hbar} (1 - t(\omega)) = \frac{e^2}{\hbar} \frac{1 - e^{iX}}{1 + \alpha f(X)}. \quad (\text{C17})$$

Since  $t(\omega) = e^{i\theta(\omega)}$  because of energy conservation and of the absence of dynamical degrees of freedom in the classically driven top-gate,  $R_K Y(\omega) = 1 - t(\omega)$  spans a circle of radius 1 centered on 1 in the complex plane [96]. Its low frequency expansion

$$R_K Y(\omega) \simeq -i \frac{\omega l/v_F}{1 + \alpha} + \frac{1}{2} \frac{(\omega l/v_F)^2}{(1 + \alpha)^2} + \dots \quad (\text{C18})$$

up to second order corresponds to an  $RC$  circuit with resistance  $R_K/2$  and electrochemical capacitance  $C_{\mu}$  such that  $R_K C_{\mu} = l/(1 + \alpha)v_F$ .

Figure 12 shows the behavior of  $\text{Arg}(t(\omega))$  as well as of  $|R_K Y(\omega)| = |1 - t(\omega)|$  as a function of  $X = \omega l/v_F$ . The

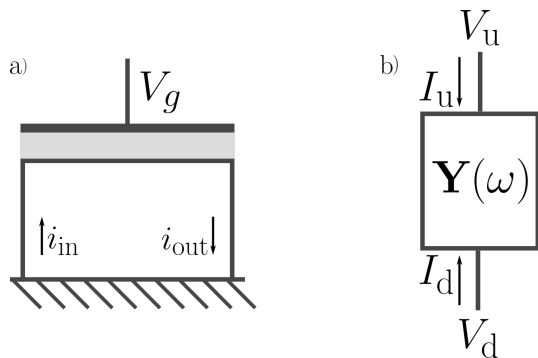


FIG. 11. (a) Folding of the edge channel capacitively coupled to the classical top gate to obtain an electrical dipole. (b) Drawing of an electrical dipole with  $\mathbf{Y}(\omega)$  its admittance matrix,  $V_u$ ,  $V_d$ ,  $I_u$  and  $I_d$  respectively denote the voltage and the average electrical current in the two connecting leads. In panel (a),  $V_u = V_g$ ,  $V_d = 0$  and  $I_d = i_{\text{in}} - i_{\text{out}}$ .

former describes how the phase of the transmission varies with  $\omega$  whereas the latter describes the filtering of the applied voltage  $V_g(\omega)$  by the top gate. As can be seen on the bottom panel of Fig. 12, the filtering exhibit a texture even at low  $\alpha$ . However, in this case, it is very similar to the filtering that would arise from applying  $V_g(t)$  to the electrons in the  $|x| \leq l/2$  region as in paragraph C 1 whereas at large  $\alpha$ , this behavior is only recovered for  $\omega \gtrsim 1/R_K C_\mu \gg v_F/l$  whereas for  $\omega R_K C_\mu \lesssim 1$ , filtering selects frequencies close to  $\omega \simeq 2\pi n v_F/l$  with  $n$  being a positive integer.

In general, the gate voltage  $V_g(t)$  is filtered into an effective time dependent voltage  $U_{\text{eff}}(t)$  via

$$U_{\text{eff}}(\omega) = \frac{V_g(\omega)}{1 + \alpha f(\omega l/v_F)} \quad (\text{C19})$$

The other effect of the top gate is to induce a non linear EMP transmission phase  $\theta(\omega)$  which is responsible for electronic decoherence beneath the top gate [45]. On the other hand, the single particle model discussed in paragraph C 1 does not lead to electronic decoherence since, in this case, Eq. (C5) corresponds to a dispersionless  $\theta(\omega) = \omega l/v_F$ .

#### Appendix D: Two counter propagating edge channels

In this Appendix, we consider the EMP scattering matrix for a model of radiation coupler involving two counter-propagating integer Quantum Hall edge channels, capacitively coupled over a region of length  $l$ . The geometric capacitance of this length  $l$  capacitor will be denoted by  $C_g$ . We assume that these two length  $l$  conductors are in total mutual influence, an hypothesis ensuring maximal coupling between them.

This modeling has been used in Ref. [97] for a rectangular quantum Hall bar of length  $l$  at filling fraction

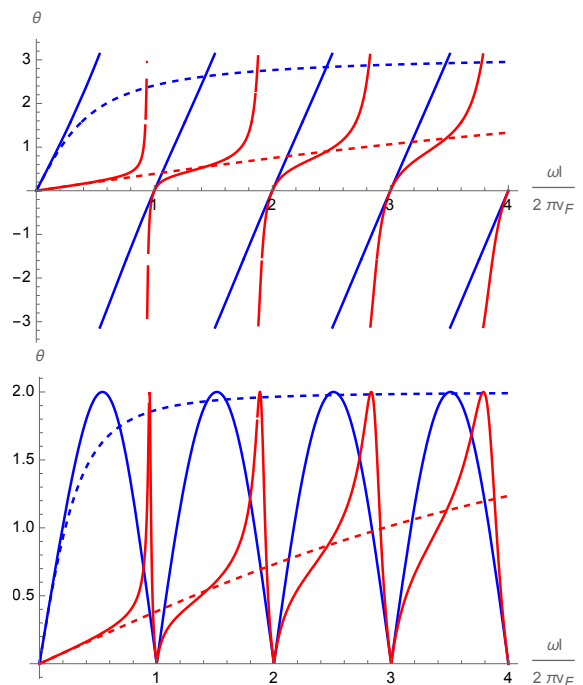


FIG. 12. Top panel: Plot of the phase  $\text{Arg}[t(\omega)]$  as a function of  $\omega l/2\pi v_F$  in the voltage locked ( $\alpha = 1/5$ , blue full line) and Coulomb blocked ( $\alpha = 15$ , red full line) regimes. In each case, the angle  $\text{Arg}[1 - R_K Y(\omega)]$  for the corresponding  $R_q C_\mu$  circuit is plotted in dashed lines with the same colors. Bottom panel: plots of  $|1 - t(\omega)|$  for the same examples as in the top panel (coloring identical to the top panel).

$\nu = 1$ . The EMP scattering matrix can thus be directly extracted from Ref. [98] and we will discuss its various limiting regimes.

#### 1. The EMP scattering matrix

Denoting by  $b$  the EMP modes of the MZI edge channels and  $a$  the EMP modes of the radiation edge channel, the EMP scattering matrix  $S(\omega)$  is given by the result of Sec. III of Ref. [98] specialized for  $\nu = 1$ :

$$S_{ba}(\omega) = S_{ab}(\omega) = \frac{-iXf(X)}{2 + \alpha f(X)} \quad (\text{D1a})$$

$$S_{aa}(\omega) = S_{bb}(\omega) = 1 - S_{ba}(\omega). \quad (\text{D1b})$$

in which  $X = \omega l/v_F$  and  $f(X) = (e^{iX} - 1)/iX$ .

The dimensionless coupling  $\alpha = C_g/C_q$  is the inverse ratio of the geometric capacitance  $C_g$  to the quantum capacitance  $C_q = e^2 l/hv_F$  of a single edge channel of length  $l$ . It reflects the strength of Coulomb interactions effects: up to a numerical factor, it is the ratio of the electrostatic energy  $e^2/2C_g$  for a single electron charge in a capacitance  $C_g$  to the kinetic energy scale  $\hbar v_F/l$  for a single electron added in a length  $l$  closed edge channel.

The regime of low  $\alpha$  ( $C_g \gg C_q$ ) is the regime where the voltage drop at the capacitor formed by the two

length  $l$  facing counter-propagating regions of length  $l$  can be neglected: both channels see the same potential. On the other hand,  $\alpha \gg 1$  is the regime of strong coupling in which Coulomb energy is so large that charging these length  $l$  regions is almost impossible. This is the Coulomb blocked regime.

We shall now discuss the limiting forms of the EMP scattering region in these two regimes. A key point in interpreting the results is the relation between the EMP scattering matrix and finite frequency impedances. Under the hypothesis of total screening, there are no current leaks to any external grounded conductor. Considering the  $b_{\text{in}}$  and  $b_{\text{out}}$  as the incoming and outgoing modes for a  $B$  lead and the  $a_{\text{in}}$  and  $a_{\text{out}}$  modes as the corresponding modes for the  $A$  leads, the finite frequency admittance of this conductor is

$$Y(\omega) = \frac{e^2}{h} S_{ba}(\omega) \quad (\text{D2})$$

At low enough frequency, this dipole can be viewed as an  $RC$  circuit with finite frequency admittance

$$Y(\omega) = -iC_\mu\omega + RC_\mu^2\omega + \mathcal{O}(\omega^3) \quad (\text{D3})$$

which leads to

$$C_\mu = \frac{C_q}{2 + \alpha} = \frac{C_q C_q / 2}{C_q / 2 + C_g} \quad \& \quad R = R_K. \quad (\text{D4})$$

We recover the expression of the quantum capacitance as the series addition of two single channel quantum capacitances (one for the  $a$  modes and the other for the  $b$  modes) with the geometric capacitance  $C_g$ . The total resistance  $R_K$  is the series addition of the two contact resistances  $R_K/2$  for the two folded edge channels.

The total screening hypothesis leads to  $S_{bb}(\omega) = 1 - S_{ba}(\omega)$ . On the other hand, energy conservation leads to  $|S_{bb}(\omega)|^2 + |S_{ab}(\omega)|^2 = 1$ . Parametrizing

$$S_{bb}(\omega) = \frac{1}{2} (1 + \xi(\omega)) \quad (\text{D5a})$$

$$S_{ba}(\omega) = \frac{1}{2} (1 - \xi(\omega)) \quad (\text{D5b})$$

thus leads to  $|\xi(\omega)| = 1$ . Consequently, the parametric plot of  $S_{ba}(\omega)$  in the complex plane is a circle of radius  $1/2$  centered on the point  $z = 1/2$ . Note that this is also the case for an  $RC$  circuit with resistance  $R_K$  and capacitance  $C_\mu$ . In the end, the EMP scattering matrix can be fully characterized by the description of the angle  $\vartheta(\omega) = \text{Arg}(\xi(\omega))$ .

Fig. 13 displays the phase  $\vartheta(\omega)$  as a function of  $\omega l/v_F$  in units of  $2\pi$  for both the voltage locked and Coulomb blocked regimes together with the graphs for the  $RC$  circuit reproducing the low frequency behavior of  $Y(\omega)$ . The probability  $|S_{ab}(\omega)|^2$  for an EMP to be transmitted from the radiation channel into the MZI upper arm is plotted in the lower panel.

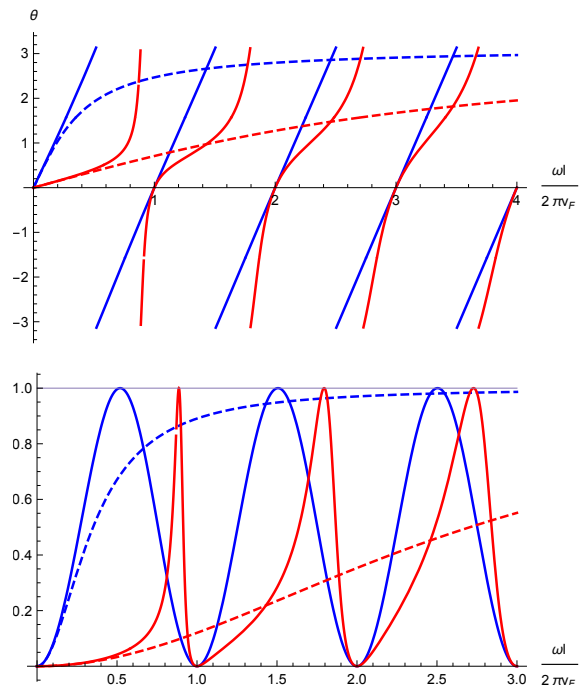


FIG. 13. Top panel: Plot of the angle  $\vartheta(\omega)$  as a function of  $\omega l/2\pi v_F$  for two different values of the coupling:  $\alpha = 1/5$  (blue full line) and  $\alpha = 15$  (red full line). For each of these values of  $\alpha$ , the angle for the  $R_K C_\mu$  circuit is plotted in dashed lines with the same colors. Bottom panel: plots of  $|S_{ba}(\omega)|^2$  for the same examples as in the top panel (coloring identical to the top panel).

## 2. The voltage locked regime

The  $\alpha \rightarrow 0$  limit of the EMP scattering matrix given by Eq. (D1) is

$$S_{ba}(\omega) = S_{ab}(\omega) = \frac{1}{2} (1 - e^{iX}) \quad (\text{D6a})$$

$$S_{aa}(\omega) = S_{bb}(\omega) = \frac{1}{2} (1 + e^{iX}). \quad (\text{D6b})$$

which therefore implies that  $\vartheta(\omega) = \omega l/v_F$ . This is consistent with the full blue line behavior displayed on the upper-panel of Fig. 13 ( $\alpha = 1/5$ ).

In this regime, the electrochemical capacitance is dominated by the quantum capacitance's contribution:  $C_\mu \simeq C_q/2$  which means that the corresponding  $RC$  time scale is  $R_K C_\mu \simeq l/2v_F$ . The fact that even at vanishing  $\alpha$ ,  $S_{ba}(\omega)$  is non-zero comes from the fact that this “weak coupling limit” is not a limit without interactions between the two counter-propagating edge channels: it only means that the voltage drop at the capacitance vanishes and that both edge channels see the same voltage. In this regime, the transmission probability exhibits sinusoidal oscillations as a function of  $\omega l/v_F$  just like a micro-wave directional coupler or two strongly coupled copropagating edge channels with local interactions would do (see Ref. [99]).

Avoiding this physically counter-intuitive behavior in the  $\alpha \ll 1$  regime requires considering a model without the total screening hypothesis. However, note that such a model would ensure a less efficient coupling between the external quantum radiation and the electrons propagating within the MZI.

### 3. The Coulomb blocked regime

Increasing  $\alpha$  introduces non-linearities in the phase  $\vartheta(\omega)$  as shown on the upper panel of Fig. 13. The electrochemical capacitance increases since it is not dominated by the geometric capacitance  $C_\mu \sim C_g$  ( $C_g \ll C_q$ ). The  $R_K C_\mu \sim R_K C_g$  time scale is then much shorter than the free electron time of flight  $R_K C_q = l/v_F$ . As a result  $1/R_K C_\mu$  increases thus explaining the flatter low frequency behavior of  $\vartheta(\omega)$  in terms of  $\omega l/v_F$  see on the upper panel of Fig. 13. The lower panel of this figure shows a strong distortion of the oscillations in the transmission probability  $|S_{ab}(\omega)|^2$  for  $\omega R_K C_\mu \lesssim 1$ . It still reaches unity for  $\omega l/v_F \equiv 0 \pmod{2\pi}$  but with narrow resonances for frequencies  $\omega/2\pi$  close to integer multiples of  $v_F/l$ . These resonances become broader with increasing order and the typical oscillations of a micro-wave directional coupler are recovered for  $\omega R_K C_\mu \gtrsim 1$ .

Consequently, at low energy  $\omega \lesssim 2\pi l/v_F$ , there is almost no EMP scattering amplitude in the very large coupling limit and the EMP transmission amplitude corresponds to a vanishing time of flight across the length  $l$  interaction region. This is the result of the zero charge constraint at infinite coupling: every charge density disturbance has to go out of the interaction region immediately and leads to no charge density change within the interaction region (hence the vanishing inter-channel EMP scattering amplitude).

At higher  $\omega$ , the modulus of decoherence amplitude goes down at each resonance which becomes broader at higher  $\omega$ . This comes from the frequency selectivity of the radiation coupler for a finite but large  $\alpha$ : it can transmit photons only at the resonances shown on the lower panel of Fig. 13. This is an interesting feature for building a frequency selective detector, the narrowest resonance being the first one for  $\omega/2\pi = l/v_F$ .

When  $\omega R_K C_\mu \gtrsim 1$ , the directional coupler behavior expected in the voltage locked regime of the previous Section is recovered. This is the regime where EMP modes have enough energy to overcome the Coulomb energy  $e^2/2C_g$ .

### Appendix E: Derivation of the radar equation

In this Appendix, the single radar equation for the outgoing average electrical current is derived. We will first derive it within the framework of time dependent

single particle scattering theory (linear electron quantum optics) using a technique which can then be adapted to the presence of Coulomb interaction effects which belong to the non-linear regime of electron quantum optics.

#### 1. Time-dependent single particle scattering approach

We consider a MZI as depicted on Fig. 1-(a) and discussed in Sec. II B. Let us recall that the single electron scattering matrices of the two QPC are assumed to be energy independent and given by:

$$S_\alpha = \begin{pmatrix} \sqrt{T_\alpha} & i\sqrt{R_\alpha} \\ i\sqrt{R_\alpha} & \sqrt{T_\alpha} \end{pmatrix} \quad (\text{E1})$$

in which  $T_\alpha$  and  $R_\alpha$  respectively denote the transmission and reflection probabilities at QPC  $\alpha = A$  or  $B$  ( $T_\alpha + R_\alpha = 1$ ).

The main idea is to express the outgoing electron field in branch 1 in terms of incoming fields by back-tracing it from the output to the input of the MZI interferometer. Assuming free propagation long the branch 2, with time of flight  $\tau_2$  leads to

$$\psi_{1\text{out}}(t) = \sqrt{T_B} \psi_{1,B_-}(t) + i\sqrt{R_B} \psi_{2,B_-}(t) \quad (\text{E2a})$$

$$= i\sqrt{R_B} e^{-i\phi_{AB}/2} \left( \sqrt{T_A} \psi_{2\text{in}}(t - \tau_2) + i\sqrt{R_A} \psi_{1\text{in}}(t - \tau_2) \right) \quad (\text{E2b})$$

$$+ \sqrt{T_B} e^{i\phi_{AB}/2} \psi_{1,B_-}(t) \quad (\text{E2c})$$

in which  $\psi_{\alpha,B_-}(t)$  denotes the fermionic field right before the QPC  $B$  and  $\psi_{\alpha\text{in}}(t)$  denotes the incoming fields right before QPC  $A$ . Equation (E2c) involves the outgoing fermionic field from the radiation coupler. In the case where propagation within this region can be described by a time dependent linear scattering, we can relate it linearly to the incoming field  $\psi_{1,A_+}$  by

$$\psi_{1,B_-}(t) = \int_{\mathbb{R}} R(t,t') \psi_{1,A_+}(t') dt' \quad (\text{E3})$$

which assumes that no electron can be injected from any other channel than the branch 1 of the MZI[100]. This enables us to write down the fully general expression for the outgoing electrical current  $i_{1\text{out}}(t) = -ev_F : (\psi_{1\text{out}}^\dagger \psi_{1\text{out}}) : (t)$  in terms of the incoming electronic fields. We obtain the outgoing current operator  $i_{1\text{out}}(t)$  as

$$i_{1\text{out}}(t) = \widehat{I}_0(t) - e \left( e^{i\varphi_{AB}} \widehat{I}_+(t) + e^{-i\varphi_{AB}} \widehat{I}_-(t) \right) \quad (\text{E4})$$

in which, at the operator level

$$\hat{I}_+(t) = -i\sqrt{T_B R_B} \int_{\mathbb{R}} R(t, t') \left[ \sqrt{T_A} \psi_{2_{in}}^\dagger - i\sqrt{R_A} \psi_{1_{in}} \right] (t - \tau_2) \left[ \sqrt{T_A} \psi_{1_{in}} + i\sqrt{R_A} \psi_{2_{in}} \right] (t') dt'. \quad (\text{E5})$$

When computing the average current, only terms that contain the same numbers of  $\psi_{\alpha_{in}}^\dagger$  and  $\psi_{\alpha_{in}}$  are retained since the MZI is fed by two independent electron sources. Consequently the AB-flux dependent part of the average current is  $\langle I_+(t) \rangle = -e\sqrt{R_A T_A R_B T_B} X_+(t)$  where

$$X_+(t) = \int_{\mathbb{R}} R(t, t') \left( \mathcal{G}_{1_{in}}^{(e)} - \mathcal{G}_{2_{in}}^{(e)} \right) (t'|t - \tau_2) dt'. \quad (\text{E6})$$

This is the time domain electron radar equation given by Eq. (22). Note that, within the single particle scattering formalism, this equation is valid for any electron source, not necessarily emitting a single electron excitation.

## 2. The interacting case

### a. The EMP scattering approach

Let us now consider the case where Coulomb interactions cannot be neglected within the radiation coupler. We shall model it using the EMP scattering formalism discussed in Sec. III A.

Note that the starting point of Eq. (E2) is still valid. But, contrary to the previous paragraph, the main challenge is now to backtrack the fermionic field along the branch 1 of the MZI. Equivalently, we have to express  $\psi_{1, B_-}(t)$  in terms of the incoming fields  $\psi_{\alpha_{in}}$  for  $\alpha = 1, 2$ . In order to do so, we consider the fermionic field  $\psi_{1, B_-}(t)$ , expressed it in terms of the outgoing EMP modes and use the EMP scattering matrix to express it in terms of the incoming modes into the radiation coupler.

To simplify the notation, the EMP modes along the branch 1 of the MZI will be denoted by  $b_\alpha(\omega)$  with  $\alpha = \text{in}$  or  $\alpha = \text{out}$  depending whether they are incoming (position  $A_+$ ) or outgoing (position  $B_-$ ). In the same way, the electromagnetic modes within the radiation channel are denoted by  $a_\alpha(\omega)$ . The scattering matrix describing the coupling between the edge channel and the electromagnetic modes is

$$S(\omega) = \begin{pmatrix} S_{bb}(\omega) & S_{ba}(\omega) \\ S_{ab}(\omega) & S_{aa}(\omega) \end{pmatrix} \quad (\text{E7})$$

so that

$$\begin{pmatrix} b_{\text{out}}(\omega) \\ a_{\text{out}}(\omega) \end{pmatrix} = S(\omega) \begin{pmatrix} b_{\text{in}}(\omega) \\ a_{\text{in}}(\omega) \end{pmatrix} \quad (\text{E8})$$

Using the bosonization formula for the fermionic field, (see Eq. (B6)) and back-propagating the bosonic mode operators across the radiation coupler,  $\psi_{1, \text{out}}(t)$  can be expressed as

$$\psi_{1, B_-}(t) = e^{i\Theta} \psi_{1, A_+}(t) D_{b_1}[(S_{bb}^* - 1)\Lambda(t)] \otimes D_a[S_{ba}^* \Lambda(t)] \quad (\text{E9})$$

where the phase  $\Theta$  is independent from  $t$ . Therefore, we need to compute the correlator  $\mathcal{G}_{\rho_i, B_-}^{(e)}(1, t|2, t)$  which is equal to

$$\langle \psi_{2, A_+}^\dagger(t - \tau_2) \psi_{1, A_+}(t) D_{b_1}[(S_{bb}^* - 1)\Lambda(t)] D_a[S_{ba}^* \Lambda(t)] \rangle \quad (\text{E10})$$

in which the correlator is taken over the incoming many-body state  $\rho_i = \rho_S \otimes \rho_{\text{em}}$  which is the tensor product of the many body electronic state  $\rho_S$  injected by the source by the incoming radiation state  $\rho_{\text{em}}$  for the  $a(\omega)$  modes.

### b. The Franck-Condon factor

Let us now discuss how the correlator (E10) can be evaluated. First of all, the part that depends on the incident radiation state  $\rho_{\text{em}}$  can be singled out thanks to the identity:

$$\langle D_a[S_{ba}^* \Lambda(t)] \rangle_{\rho_{\text{em}}} = \langle D_a[S_{ba}^* \Lambda(t)] \rangle_{|0\rangle} \times \langle : D_a[S_{ba}^* \Lambda(t)] : \rangle_{\rho_{\text{em}}} \quad (\text{E11})$$

in which we have introduced the bosonic normal ordering  $: \dots :$ . All the dependence in the incident radiation state  $\rho_{\text{em}}$  is thus contained in the average value of the normal ordered displacement operator  $: D_a[S_{ba}^* \Lambda(t)] :$  for the  $a(\omega)$  modes. The average value  $\langle D_a[S_{ba}^* \Lambda(t)] \rangle_{|0\rangle}$  is taken over the vacuum state for the  $a(\omega)$  modes which means that it can be reabsorbed into the correlator given by Eq. (E10) except that this time the quantum average is taken over the state  $\rho_{S,0} = \rho_S \otimes |0\rangle \langle 0|$ . This can be summarized by

$$\mathcal{G}_{\rho_i, B_-}^{(e)}(1, t|2, t) = \mathcal{G}_{\rho_{S,0}, B_-}^{(e)}(1, t|2, t) \quad (\text{E12a})$$

$$\times \langle : D_a[S_{ba}^* \Lambda(t)] : \rangle_{\rho_{\text{em}}} \quad (\text{E12b})$$

since  $\rho_{S,0} = \rho_S \otimes |0\rangle \langle 0|$  corresponds to a situation where no incident radiation is sent onto the MZI. Therefore, the correlator  $\mathcal{G}_{\rho_{S,0}, B_-}^{(e)}(1, t|2, t)$  is exactly the one appearing when computing the average current flowing out of the MZI in the absence of electromagnetic radiation sent onto it via the  $a(\omega)$  modes. This problem corresponds to the problem of electronic decoherence within the MZI.

In the end, the effect of the radiation injected into the radiation coupler is described by the factor

$$\mathcal{F}_{\rho_{\text{em}}}(t) = \langle : D_a[S_{ba}^* \Lambda(t)] : \rangle_{\rho_{\text{em}}} \quad (\text{E13})$$

which is the exact analogous of the Franck-Condon factor that appears in the spectroscopy of complex molecules [46].

c. *Electronic propagation contribution*

The electronic coherence  $\mathcal{G}_{\rho_{S,0},B_-}^{(e)}(1,t|2,t)$  is more difficult to evaluate because it corresponds to the outgoing single electron coherence after propagation across the MZI in the presence of Coulomb interactions within the branch 1 of the MZI. It turns out that simple and physically transparent expressions can be found in the case where  $S$  is an ideal single electron source. In this case, the state  $S$  is of the form

$$\rho_S = \psi_{1\text{in}}^\dagger[\varphi_e] |F\rangle \langle F| \psi_{1\text{in}}[\varphi_e] \quad (\text{E14})$$

$$\mathcal{G}_{\rho_{S,0},B_-}^{(e)}(1,t|2,t) = -i\sqrt{R_A T_A} \times \langle F, 0_a | \psi_{2,A_+}[\varphi_e] \psi_{2,A_+}^\dagger(t - \tau_2) \psi_{1,B_-}(t) \psi_{1,A_+}^\dagger[\varphi_e] |F, 0_a\rangle \quad (\text{E15a})$$

$$= -i\sqrt{R_A T_A} \times \langle F_2 | \psi_{2,A_+}[\varphi_e] \psi_{2,A_+}^\dagger(t - \tau_2) |F_2\rangle \times \langle F_1, 0_a | \psi_{1,B_-}(t) \psi_{1,A_+}^\dagger[\varphi_e] |F_1, 0_a\rangle \quad (\text{E15b})$$

in which  $|F, 0_a\rangle$  denotes the tensor product of the Fermi sea in both branches of the MZI and the ground state for the environmental modes. Since  $\varphi_e$  is an electronic excitation above the Fermi level, the contribution associated with propagation along the branch 2 of the MZI can be readily evaluated:

$$\langle \psi_{2,A_+}[\varphi_e] \psi_{2,A_+}(t - \tau_2) \rangle_{|F_2\rangle} = \varphi_e(t - \tau_2)^*. \quad (\text{E16})$$

We are thus left with evaluating:

$$\langle \psi_{1,B_-}(t) \psi_{1,A_+}^\dagger[\varphi_e] \rangle_{|F_1,0_a\rangle} = \int_{\mathbb{R}} v_F \varphi_e(t') \langle \psi_{1,B_-}(t) \psi_{1,A_+}(t') \rangle_{|F_1,0_a\rangle} dt'. \quad (\text{E17})$$

The time domain amplitude

$$\mathcal{Z}_1(\tau) = v_F \langle \psi_{1,B_-}(\tau) \psi_{1,A_+}^\dagger(0) \rangle_{|F_1,0_a\rangle} \quad (\text{E18})$$

is the elastic single electron scattering amplitude across the branch 1 of the MZI. It is related to the elastic scattering amplitude  $\tilde{\mathcal{Z}}_1(\omega)$  computed in Refs. [44, 58] by a Fourier transform:

$$\mathcal{Z}_1(\tau) = \int_0^{+\infty} \tilde{\mathcal{Z}}_1(\omega) e^{-i\omega\tau} \frac{d\omega}{2\pi}. \quad (\text{E19})$$

Evaluating  $\tilde{\mathcal{Z}}_1(\omega)$  can be done using the expressions given in Ref. [45, 101] which we recall here for completeness:

$$\tilde{\mathcal{Z}}_1(\omega) = 1 + \int_0^\omega B(\omega') d\omega' \quad (\text{E20})$$

in which  $B(\omega)$  is the solution of the integral equation

$$\omega B(\omega) = S_{bb}(\omega) - 1 + \int_0^\omega B(\omega') (S_{bb}(\omega') - 1) d\omega' \quad (\text{E21})$$

with initial condition  $B(0^+) = (dS_{bb}/d\omega)(\omega = 0^+)$ . Finally, we obtain:

$$\langle \psi_{1,B_+}(t) \psi_{1,A_+}^\dagger[\varphi_e] \rangle_{|F_1,0_a\rangle} = \int_{\mathbb{R}} \varphi_e(t') \mathcal{Z}_1(t - t') dt'. \quad (\text{E22})$$

where  $|F\rangle$  corresponds to the Fermi sea with chemical potential  $\mu = 0$  in the two incoming electronic channels of the MZI and  $\psi_{1\text{in}}^\dagger[\varphi_e]$  creates a single electron excitation with wave function  $\varphi_e$  injected into the MZI (position  $A_-$ ).

Expressing  $\psi_{1\text{in}}^\dagger[\varphi_e]$  in terms of  $\psi_{1,A_+}^\dagger[\varphi_e]$  and  $\psi_{2,A_+}^\dagger[\varphi_e]$  enables us to show that

The correlator  $\langle \psi_{2,A_+}[\varphi_e] \psi_{2,B_-}^\dagger(t - \tau_2) \rangle_{|F_2\rangle}$  could also be rewritten in a similar way

$$\langle \psi_{2,A_+}[\varphi_e] \psi_{2,B_-}^\dagger(t) \rangle_{|F_2\rangle} = \int_{\mathbb{R}} \varphi_e(t')^* \mathcal{Z}_2(t - t')^* dt' \quad (\text{E23})$$

using the elastic scattering amplitude  $\mathcal{Z}_2(\tau) = \delta(\tau - \tau_2)$  corresponding to ballistic propagation during time of flight  $\tau_2$ .

Note that this form of the correlator  $\langle \psi_{2,A_+}[\varphi_e] \psi_{2,B_-}(t) \rangle$  remains valid in the presence of electronic decoherence along branch 2 of the MZI provided it is not caused by direct or indirect interactions (bath mediated) between the two branches of the MZI. This means that there must be no crosstalk between the two branches: each of these branch do interact with their own environment which are prepared in their ground states. In this case, we should use the elastic scattering amplitude  $\tilde{\mathcal{Z}}_2(\omega)$  for  $\omega > 0$  to define  $\mathcal{Z}_2(\tau)$ . The elastic scattering amplitude  $\tilde{\mathcal{Z}}_2(\omega)$  can be computed in terms of the finite frequency admittance of the branch 2.

d. *General result*

Let us finally collect the general result for the inter-branch coherence  $\mathcal{G}_{\rho_{S,0},B_-}(1,t|2,t)$  right before the second QPC in the general situation where each of the branches involves Coulomb interactions, and possibly a coupling to its own radiation channel fed by the vacuum state. In the absence of external radiation, the expression



$$v_F \mathcal{G}_{\rho_{S,0}, B_-}^{(e)}(1, t|2, t) = \int_{\mathbb{R}^2} v_F \varphi_e(t - \tau_1) \varphi_e(t - \tau_2)^* \mathcal{Z}_1(\tau_1) \mathcal{Z}_2(\tau_2) d\tau_1 d\tau_2 \quad (\text{E24})$$

has a physically transparent interpretation: each wave packet gets propagated according to the elastic scattering amplitude  $\mathcal{Z}_\alpha(\tau)$  along the corresponding branch.

In the presence of incoming radiation arriving on each radiation coupler of each branch  $\alpha$  in independent respective quantum states described by the density operators  $\rho_{\text{em},\alpha}$ , Eq. (E12) generalizes to

$$\mathcal{G}_{\rho_i, B_-}^{(e)}(1, t|2, t) = \mathcal{G}_{\rho_{S,0}, B_-}^{(e)}(1, t|2, t) \times \prod_{\alpha=1,2} \left\langle : D_{a_\alpha} \left[ \left( S_{ba}^{(\alpha)} \right)^* \Lambda(t) \right] : \right\rangle_{\rho_{\text{em},\alpha}} \quad (\text{E25a})$$

In the end, the interference signal  $X_+(t)$  is given by

$$X_+(t) = v_F \int_{\mathbb{R}^2} \varphi_e(t - \tau_1) \varphi_e(t - \tau_2)^* \times R_{\text{eff},1}(t, t - \tau_1) R_{\text{eff},2}(t, t - \tau_2) d\tau_1, d\tau_2 \quad (\text{E26})$$

in which the effective single particle scattering amplitudes are given by the product of the elastic scattering amplitude by the Franck-Condon factor:

$$R_{\text{eff},\alpha}(t, t') = \mathcal{Z}_\alpha(t - t') \mathcal{F}_{\rho_{\text{em},\alpha}}(t) \quad (\text{E27})$$

thus leading to the single electron radar equation (22) which reduces to Eq. (23) in the case of ballistic propagation in time  $\tau_2$  along branch 2 and no coupling to external radiation on this branch.

Last but not least, in the presence of Coulomb interactions, the radar equation is valid only for an incoming single electron excitation injected into the electronic MZI!

## Appendix F: Connection to full counting statistics

In the context of experiments performed on AlGaAs/AsGa systems in the quantum Hall regime, the radiation channel may also be a chiral quantum Hall edge channel, as depicted on Fig. 14-(a). In this case,  $\mathcal{F}_{\rho_{\text{em}}}(t)$  can also be interpreted in terms of a form of full counting statistics for electronic transport in the radiation channel as noticed in Ref. [102]. Since this work relied on a specific interaction model as well as on single particle scattering, we present here a full many body derivation independent on the details of the Coulomb interaction model.

When the radiation channel is a single integer quantum Hall edge channel, the incoming electrical current arriving into the interaction region via this edge channel is, for  $\omega > 0$ :

$$i_{\text{in}}(\omega) = -e\sqrt{\omega} a_{\text{in}}(\omega) \quad (\text{F1})$$

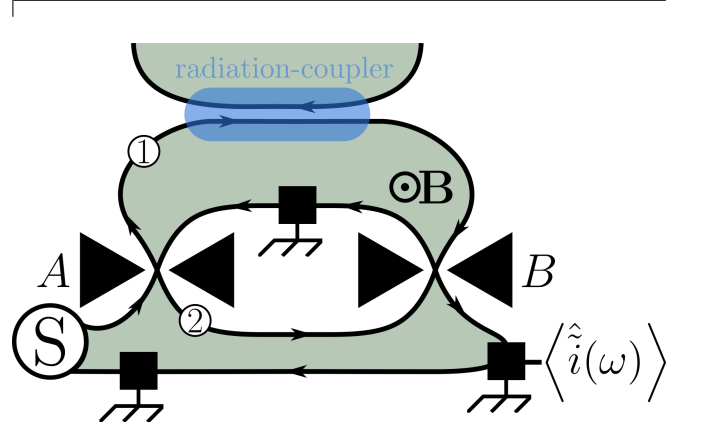


FIG. 14. (Colors online) Sample design of the electron radar using chiral edge channels in the integer quantum Hall regime (2DEG in green). The blue region where two counter-propagating quantum Hall edge channels are facing each other at short ( $\lesssim 100$  nm) distance forms a radiation coupler between the channel 1 of the MZI and the radiation channel in which the radiation to be analyzed is sent. The quantity of interest is the average outgoing current from the MZI and more precisely the first harmonic in the Aharonov-Bohm phase.

Introducing

$$\Gamma_{ba}(\tau) = \int_0^{+\infty} \frac{S_{ba}(\omega)}{-i\omega} e^{-i\omega\tau} \frac{d\omega}{2\pi} + \text{c.c.} \quad (\text{F2})$$

the normalized filtered charge operator

$$N(t) = \int_{\mathbb{R}} \Gamma_{ba}(t - \tau) \frac{i_{\text{in}}(\tau)}{-e} d\tau \quad (\text{F3})$$

associated with the windowing function  $\tau \mapsto \Gamma_{ba}(t - \tau)$  can be used to provide a compact expression for  $\mathcal{F}_{\rho_{\text{em}}}(t)$ :

$$\mathcal{F}_\rho(t) = \left\langle : e^{2\pi i N(t)} : \right\rangle_{\rho_{\text{em}}} . \quad (\text{F4})$$

The  $2\pi N(t)$  operator represents the quantum phase kicks associated with the incoming electrical current felt by a localized electron propagating within the MZI. Note that the exponential of this quantum phase kick operator is normal ordered with respect to the bosonic modes  $a_{\text{in}}(\omega)$ . One can then connect this ordering to the time ordering in order to establish the precise connection to time ordered electrical current correlators.

Finally, let us comment on the interpretation of the windowing function  $\Gamma_{ba}(t - \tau)$ . Since  $\Gamma_{ba}(\omega) = iS_{ba}(\omega)/\omega$  for  $\omega > 0$ , the relation between the EMP scattering matrix and finite frequency admittances [45, 48, 59, 60] leads to

$$\Gamma_{ba}(\omega) = \frac{S_{ba}(\omega)}{-i\omega} = \frac{R_K}{-i\omega} \frac{\partial I_b^{(\text{out})}(\omega)}{\partial V_a^{(\text{in})}(\omega)} \quad (\text{F5})$$

in which  $I_b^{(\text{out})}(\omega)$  denotes the average total current going out from the interaction region within the MZI interferometer – the propagation channel for the  $b$  EMP modes – and  $V_a^{(\text{in})}(\omega)$  denotes a classical voltage drive applied to the incoming channel of the radiation channel in which the EMP  $a$  modes propagate. This equation thus connects  $\Gamma_{ba}(\omega)$  to the finite frequency admittance of the electrical dipole associated with the interaction region. Since the coupling is purely capacitive, one expects this finite frequency response to be capacitive, that is of the form

$$\frac{\partial I_b^{(\text{out})}(\omega)}{\partial V_a^{(\text{in})}(\omega)} = -i\omega C_{ba}^{(\text{eff})}(\omega) \quad (\text{F6})$$

in which the effective frequency dependence capacitance  $C_{ba}^{(\text{eff})}(\omega)$  goes to a non zero capacitance in the low frequency limit. Consequently,  $\Gamma_{ba}(\tau)$  appears as the effective response rate associated with this capacitance

$$\Gamma_{ba}(\tau) = \int_0^{+\infty} R_K C_{ba}^{(\text{eff})}(\omega) e^{-i\omega\tau} \frac{d\omega}{2\pi} + \text{c.c.} \quad (\text{F7})$$

### Appendix G: The radar equation in the frequency domain

Let us introduce

$$\tilde{R}(\omega_+, \omega_-) = \int_{\mathbb{R}^2} R(t, t') e^{i(\omega_+ t - \omega_- t')} dt dt' \quad (\text{G1})$$

which is directly proportional to the amplitude for scattering an incoming electron at energy  $\hbar\omega_-$  to the energy  $\hbar\omega_+$ . Denoting by  $\tilde{X}_+(\omega)$  the Fourier transform of the signal  $X_+(t)$  at frequency  $\omega/2\pi$ , Eq. (22) then takes the form

$$\tilde{X}_+(\omega) = \int_{\mathbb{R}^2} v_F \Delta \tilde{\mathcal{G}}_S^{(e)}(\omega_-, \omega_+ - \omega) e^{i(\omega - \omega_+) \tau_2} \tilde{R}(\omega_+, \omega_-) \frac{d\omega_+ d\omega_-}{(2\pi)^2} \quad (\text{G2})$$

in which

$$\Delta \tilde{\mathcal{G}}_\rho^{(e)}(\omega_+ | \omega_-) = \int_{\mathbb{R}^2} \Delta \mathcal{G}_\rho^{(e)}(t | t') e^{i(\omega_+ t - \omega_- t')} dt dt' \quad (\text{G3})$$

denotes the excess single electron coherence in the frequency domain. Eq. (G2) determines the interference contribution to the finite frequency average electrical current in the  $I_{\text{out}}$  branch of the MZI.

Its physical interpretation is quite clear: for  $\omega > 0$ , the average finite frequency current  $\langle i_{I_{\text{out}}}(\omega) \rangle$  probes the outgoing electronic coherence between  $\omega_+$  and  $\omega_+ - \omega$  for all  $\omega_+$ . The latter is propagating along the branch 2 of the MZI with time of flight  $\tau_2$ , hence picking a phase  $e^{i(\omega_+ - \omega)\tau_2}$ . Since it appears in the complex conjugated amplitude, this leads to the phase factor  $e^{i(\omega - \omega_+)\tau_2}$  in

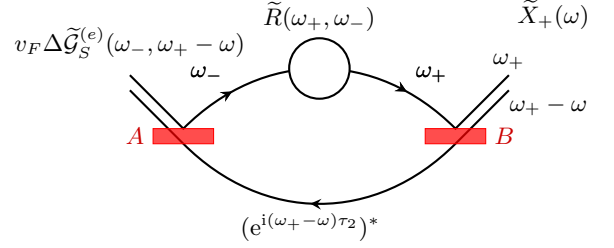


FIG. 15. Physical interpretation of the linear radar equation (G2) in the frequency domain showing the contribution of incoming single electron coherence in the frequency domain to  $\tilde{X}_+(\omega)$  for  $\omega > 0$ . Definition of the two paths is the same as in Fig. 5.

Eq. (G2). On branch 1 of the MZI, the electron enters the radiation coupler with energy  $\hbar\omega_-$  and exits with energy  $\hbar\omega_+$  with an amplitude  $\tilde{R}(\omega_+, \omega_-)$ . Therefore, the contribution of the outgoing coherence between  $\omega_+$  and  $\omega_+ - \omega$  comes from an incoming coherence between  $\omega_-$  and  $\omega_+ - \omega$  emitted by the source  $S$  as summarized on Fig. 15.

### Appendix H: Limiting regimes of the single radar equation

We now discuss the limiting regimes of a time or of a frequency resolved single electron excitation. The resulting limiting form of the electron radar equation will be relevant whenever the time (resp. frequency) extension of the probe is much smaller than the typical time (resp. frequency) length scales of the effective scattering matrix. As expected, time resolved wave packets are well suited to explore the time dependence of the scattering whereas energy resolved excitations gives access to the scattering amplitude in the frequency domain.

#### 1. Energy resolved probes

We consider an resolved excitation with Gaussian line-shape, centered at energy  $\hbar\omega_e$  and with linewidth  $\gamma_e \gg |\omega_e|$ . Its wave function in the energy domain, defined by Eq. (A6) is:

$$\tilde{\varphi}_e(\omega) = \mathcal{N} \Theta(\text{sign}(\omega_e) \omega) e^{-(\omega - \omega_e)^2 / 2\gamma_e^2} \quad (\text{H1})$$

where the normalization condition (A7) gives [103]  $\mathcal{N}^2 \gamma_e / v_F \sqrt{4\pi} \simeq 1$ . For  $\omega_e > 0$  we are dealing with an electronic excitation, whereas for  $\omega_e < 0$  we are dealing with a hole excitation. In the limit where  $\gamma_e \ll |\omega_e|$  is much smaller than the scales of variation of  $\tilde{R}(\omega_+, \omega_-)$ , the electron radar signal in the frequency domain given by Eq. (G2) then gives

$$\tilde{X}_+(\omega; \tau_2) \simeq \frac{\gamma_e}{\sqrt{\pi}} e^{-i\omega_e \tau_2} \tilde{R}(\omega + \omega_e, \omega_e). \quad (\text{H2})$$

Whenever  $\omega_e$  and  $\omega + \omega_e$  have the same sign, we are accessing the electron to electron or hole to hole effective scattering whereas whenever  $\omega_e$  and  $\omega + \omega_e$  do not have the same sign, we are accessing electron to hole or hole to electron effective scattering.

## 2. Time resolved probes

We consider a normalized Gaussian single electron wave packet:

$$\varphi_{\text{tr}}(t) = \frac{1}{\sqrt{v_F \sigma_e \sqrt{\pi}}} e^{-(t-t_e)^2/2\tau^2} \quad (\text{H3})$$

with  $t_e$  the emission time and  $\tau_e$  the duration of the single electron wave packet. Using Eq. (22) to compute the average time dependent current and brutally taking the limit  $\sigma_e \rightarrow 0$  leads to, at first order in  $\sigma_e$ :

$$X_+(t) \simeq \tau_e R(t_e + \tau_2, t_e) \delta(t - \tau_2 - t_e) \quad (\text{H4})$$

The condition  $t = t_e + \tau_2$  comes from ballistic propagation along the reference arm of the MZI and,  $X_+(t)$  is then proportional to the amplitude for the electron to enter branch 1 at  $t_e$  and exit it at time  $t$ .

However, this naive computation does not take into account the constraint that the incoming single electron excitation must be restricted to positive energies due to the presence of the Fermi sea which is not the case for the wave packet considered in Eq. (H3). Introducing a finite energy shift via the factor  $e^{-i\omega_e(t-t_e)}$  in front of the r.h.s of Eq. (H3) with  $\omega_e \gg 2\pi v_F/\tau_e$  leads to a wave packet with negligible weight at negative energies. But this introduces a rapidly oscillating term  $e^{-i\omega_e(t-t'-\tau_2)}$  in front of  $R(t, t') = \mathcal{Z}_1(t-t')\mathcal{F}_{\rho_{\text{em}}}(t)$  in the radar equation (22). This means that we are probing electronic decoherence at energies close to  $\hbar\omega_e$ . But, as shown in Ref. [101], electronic decoherence is expected to be worse at high energies and may indeed kill the interference signal.

In order to mitigate this problem, the proper approach consists of introducing electronic wave packets that are close to the Fermi surface and well localized in space such as the Leviton. This is discussed in Appendix I.

## Appendix I: Fringe contrast for Levitons

Let us consider the case of a Leviton wave-packet of width  $\tau_e$ . Its wave function is Lorentzian in the time domain and exponential in the frequency domain [104]. We are interested in the interference contribution to the outgoing electrical current for a Leviton of duration  $\tau_e$  injected at time  $t_e$ .

Because of the simple expression for the Leviton wave packet in the frequency domain, the electron radar equation in the frequency domain (see Eq. (G2)) gives us a

convenient form for  $X_+^{(\text{dc})}$  suitable for numerical evaluations:

$$X_+^{(\text{dc})} = \int_{\mathbb{R}} \tilde{\mathcal{F}}_{\rho_{\text{em}}}(\Omega) e^{-i\Omega(t_e+\tau_2)} f_{\tau_e, \tau_2}(\Omega) \frac{d\Omega}{2\pi} \quad (\text{I1})$$

in which the filter

$$f_{\tau_e, \tau_2}(\Omega) = 4\pi\tau_e \int_{|\Omega|/2}^{+\infty} \tilde{\mathcal{Z}}_1\left(\omega - \frac{\Omega}{2}\right) e^{-2\omega\tau_e} e^{-i(\omega - \frac{\Omega}{2})\tau_2} \frac{d\omega}{2\pi} \quad (\text{I2})$$

contains all the effects of electronic decoherence along branch 1 and ballistic propagation along branch 2 of the interferometer.

Because the elastic scattering amplitude  $\tilde{\mathcal{Z}}_1(\omega)$  tends to decrease in modulus with increasing  $\omega$ ,  $f_{\tau_e, \tau_2}(\Omega)$  is expected to be a low pass filter. The limit  $\tau_e \rightarrow 0^+$  may even lead to vanishing signal since, in the case of the two counter-propagating edge channel model considered in Appendix D, a very short Leviton may experience fractionalization as it flies across the radiation coupler. For short wave packets, this would kill the electronic interference signal. In the absence of external radiation, since  $\mathcal{F}_{|0\rangle}(t) = 1$ , we obtain

$$\left[X_+^{(\text{dc})}\right]_{|0\rangle} = 4\pi\tau_e \int_0^{+\infty} \tilde{\mathcal{Z}}_1(\omega) e^{-2\omega\tau_e} e^{-i\omega\tau_2} \frac{d\omega}{2\pi}. \quad (\text{I3})$$

This quantity, which does not anymore depend on  $t_e$  but depends on  $\tau_2$  represents the base interference contribution for the dc outgoing current from the MZI.

## Appendix J: Squeezing detection

This appendix presents the computations of the Franck-Condon factor in the case of a time periodic noise, with specialization to narrow band squeezed noise. We first briefly recall the structure of a single mode squeezed vacuum for pedagogy and then proceed to the discussion of time-periodic noise. In Sec. J2, we show that such a noise can exhibit sub-vacuum fluctuations coming from two-mode squeezing in a narrow band around a given frequency  $\omega_0/2\pi$ . The harmonic structure of the resulting Franck-Condon factor is then discussed in Sec. J3.

### 1. Squeezed vacuum in a single mode

In this Appendix, we recall the basics needed to describe the squeezed vacuum for a single mode[105]:

$$|\text{Sq}_z\rangle = e^{z(a^\dagger)^2 - z^* a^2} |0\rangle \quad (\text{J1})$$

where  $a$  and  $a^\dagger$  are the creation and destruction operators for a single mode and  $z \in \mathbb{C}$ . The squeezing operator  $\mathbb{S}_z$  equal to  $e^{z(a^\dagger)^2 - z^* a^2}$ , performs a Bogoliubov transformation on the original mode operators:

$$\mathbb{S}_z^\dagger a \mathbb{S}_z = \cosh(2|z|) a + e^{i\varphi} \sinh(2|z|) a^\dagger. \quad (\text{J2})$$

This enables us to compute the expectation value of any products of  $a$  and  $a^\dagger$  in the state  $|\text{Sq}_z\rangle$  as the expectation value of the same expression in terms of the Bogoliubov transformed operators

$$a_z = \cosh(2|z|) a + e^{i\varphi} \sinh(2|z|) a^\dagger \quad (\text{J3a})$$

$$a_z^\dagger = \cosh(2|z|) a^\dagger + e^{i\varphi} \sinh(2|z|) a \quad (\text{J3b})$$

where  $\varphi = \text{Arg}(z)$ . More precisely

$$\langle \mathcal{O}[a, a^\dagger] \rangle_{|\text{Sq}_z\rangle} = \langle \mathcal{O}[a_z, a_z^\dagger] \rangle_{|0\rangle} \quad (\text{J4})$$

Applying this relation to the quadrature

$$X_\vartheta = \frac{1}{\sqrt{2}} (e^{i\vartheta} a + e^{-i\vartheta} a^\dagger) \quad (\text{J5})$$

leads to  $\langle X_\vartheta \rangle_{|\text{Sq}_z\rangle} = 0$  and

$$\langle (\Delta X_\vartheta)^2 \rangle_{|\text{Sq}_z\rangle} = \frac{1}{2} + \sinh^2(2|z|) \quad (\text{J6a})$$

$$+ \cosh(2|z|) \sinh(2|z|) \cos(2\vartheta + \varphi) \quad (\text{J6b})$$

which shows that the fluctuations are anisotropic in the Fresnel plane and that  $\text{Arg}(z)$  determines the principal axes of the ellipsoid of fluctuations. Its extrema are:

$$\max_\vartheta \langle (\Delta X_\vartheta)^2 \rangle_{|\text{Sq}_z\rangle} = \frac{1}{2} e^{4|z|} \quad (\text{J7a})$$

$$\min_\vartheta \langle (\Delta X_\vartheta)^2 \rangle_{|\text{Sq}_z\rangle} = \frac{1}{2} e^{-4|z|} \quad (\text{J7b})$$

The vacuum fluctuations being given by  $1/2$ , the state  $|\text{Sq}_z\rangle$  appears as squeezed with sub-vacuum fluctuations compressed at most by a factor  $e^{-4|z|} < 1$  as soon as  $|z| \neq 0$ . Note that with  $\vartheta = \omega_0 t$ , we recover the  $2\omega_0$  oscillations of the fluctuations of harmonic mode of energy  $\hbar\omega_0$ .

Since the isotropic part of the fluctuations corresponds to  $\frac{1}{2} + \langle a^\dagger a \rangle_{|\text{Sq}_z\rangle}$ , Eq. (J6a) determines the average photon number in the squeezed vacuum  $|\text{Sq}_z\rangle$ :

$$\langle a^\dagger a \rangle_{|\text{Sq}_z\rangle} = \sinh^2(2|z|) \quad (\text{J8})$$

Thinking of this harmonic mode as an optical mode, the above discussion shows that increasing the squeezing parameter  $z$  increases the average number of photons. A squeezed vacuum is thus on average more noisy than the true vacuum even if increasing  $|z|$  decreases its minimal fluctuations.

## 2. Narrow band time periodic noise

Let us consider a time periodic current noise with period  $\pi/\omega_0$  which, as discussed in the previous paragraph, is natural for squeezing around a frequency  $\omega_0/2\pi$ . This is more natural in the spirit of mesoscopic physics where the radiation source may be a periodically driven conductor at a given frequency which would, by time translation invariance, generate a radiation whose correlators have the same time periodicity.

We then consider the simplest correlation structure for the creation and destruction operators  $a(\omega)$  and  $a^\dagger(\omega)$  that satisfies both the requirement of  $\pi/\omega_0$  periodicity as well as the requirement that its time-averaged power spectrum is concentrated in a narrow band around  $\omega_0$ . This leads to [106] ( $\omega_\pm > 0$ ):

$$\langle a^\dagger(\omega_-) a(\omega_+) \rangle = \delta(\omega_+ - \omega_-) \bar{n}(\omega) \quad (\text{J9a})$$

$$\langle a(\omega_-) a(\omega_+) \rangle = \delta(\omega_+ + \omega_- - 2\omega_0) \xi \left( \frac{\omega_+ - \omega_-}{2} \right) \quad (\text{J9b})$$

where  $\bar{n}(\omega) \geq 0$  denotes the average photon number in the mode at  $\omega$  and  $\xi(\Omega)$  denotes the average photon pair correlation between the modes at frequencies  $\omega_0 + \Omega$  and  $\omega_0 - \Omega$ . In the narrow band situation where the emitted power density  $\hbar\omega \bar{n}(\omega)$  is concentrated near  $\omega_0$ ,  $\bar{n}(\omega) \neq 0$  only for  $|\omega - \omega_0| \lesssim \gamma_0/2$  and  $|\xi(\Omega)| \neq 0$  only for  $|\Omega| \lesssim \gamma_0/2$ . Note that the  $\delta$ -function constraints in these equations arises from time periodicity as well as from Cauchy Schwartz inequalities (see Ref. [38] for analogous considerations in the context of electron quantum optics).

Substituting these correlators in Eq. (41) leads to:

$$|\mathcal{F}_{\rho_{\text{em}}}(t)| = e^{\Re[\xi_{\text{eff}} e^{-2i\omega_0 t}] - N_{\text{eff}}} \quad (\text{J10})$$

in which

$$N_{\text{eff}} = \int_0^{+\infty} \frac{|S_{ba}(\omega)|^2}{\omega} \bar{n}(\omega) d\omega \quad (\text{J11a})$$

$$\xi_{\text{eff}} = \int_{-\omega_0}^{+\omega_0} \frac{S_{ba}(\omega_0 + \Omega) S_{ba}(\omega_0 - \Omega)}{\sqrt{\omega_0^2 - \Omega^2}} \xi(2\Omega) d\Omega. \quad (\text{J11b})$$

In the narrow band approximation in which  $\bar{n}(\omega) = \bar{n}$  for  $|\omega - \omega_0| \leq \gamma_0/2$ ,  $\xi(\Omega) = \xi$  for  $|\Omega| \leq \gamma_0/2$  and where the frequency dependence of  $S_{ba}(\omega)$  around  $\omega_0$  is neglected, we obtain

$$N_{\text{eff}} = |S_{ba}(\omega_0)|^2 \frac{\gamma_0}{\omega_0} \bar{n} \quad (\text{J12a})$$

$$\xi_{\text{eff}} = |S_{ba}(\omega_0)|^2 \frac{\gamma_0}{\omega_0} e^{2i\text{Arg}(S_{ba}(\omega_0))} \xi \quad (\text{J12b})$$

Two mode squeezing between  $\omega_0 + \Omega/2$  and  $\omega_0 - \Omega/2$  for all  $|\Omega| \leq \gamma_0$  leads to

$$\bar{n} = \sinh^2(2|z|) \quad (\text{J13a})$$

$$|\xi| = \sinh(4|z|)/2 \quad (\text{J13b})$$

where  $z$  is the squeezing parameter, assumed to be the same for all these pairs of modes. Substituting this into Eqs. (J12) and the result into (J10) then leads to Eq. (43).

### 3. Harmonic decomposition

We now decompose the time periodic Franck-Condon factor given by Eq. (43) in Fourier series:

$$\mathcal{F}_{\text{Sq}_z}(t) \simeq e^{-\Lambda \sinh^2(2|z|)} \times \sum_{n \in \mathbb{Z}} I_{|n|}(\Lambda \cosh(2|z|) \sinh(2|z|)) e^{-2in\omega_0(t-\tilde{t}_e)} \quad (\text{J14})$$

where  $\Lambda = |S_{ba}(\omega_0)|^2/Q_0$  and  $I_n$  denotes the modified Bessel function of order  $n$ . The time  $\tilde{t}_e$  arises from the phase of  $S_{ba}(\omega_0)$  as well as of the squeezing parameter. We will forget it in the following since it can be absorbed in a redefinition of the Leviton's injection times.

Because  $|S_{ba}(\omega_0)|^2 \leq 1$  and  $Q_0$  is significantly larger than 1,  $\Lambda \ll 1$ . Remembering also that experimentally reachable squeezing factors are not very high ( $|z| \simeq 0.1755$  for 3dB squeezing) and therefore,  $\Lambda \cosh(2|z|) \sinh(2|z|) \lesssim 1$ . Moreover,  $I_n(x) \simeq (x/2)^n/n!$  for  $n \geq 1$ . Consequently, the most important contribution comes from the first harmonics:  $n = 0$  and  $n = \pm 1$  in Eq. (J14). Retaining only these leads to:

$$\mathcal{F}_{\text{Sq}_z}(t) \simeq \mathcal{F}_0(z, \Lambda) + e^{-2i\omega_0 t} \mathcal{F}_1(z, \Lambda) + e^{2i\omega_0 t} \mathcal{F}_{-1}(z, \Lambda) \quad (\text{J15})$$

where, at the lowest non-trivial order in  $\Lambda$ :

$$\begin{aligned} \mathcal{F}_0(z, \Lambda) &= e^{-\Lambda \sinh^2(2|z|)} I_0(\Lambda \cosh(2|z|) \sinh(2|z|)) \\ &\simeq 1 - \Lambda \sinh^2(2|z|) + \mathcal{O}(\Lambda^2) \end{aligned} \quad (\text{J16a})$$

$$\begin{aligned} \mathcal{F}_{\pm 1}(z, \Lambda) &= e^{-\Lambda \sinh^2(2|z|)} I_{\pm 1}(\Lambda \cosh(2|z|) \sinh(2|z|)) \\ &\simeq \frac{\Lambda}{2} \cosh(2|z|) \sinh(2|z|) + \mathcal{O}(\Lambda^2). \end{aligned} \quad (\text{J16b})$$

The  $n = 0$  harmonic contains the contrast obtained when averaging over the emission time  $t_e$ :

$$\overline{[X_+^{(\text{dc})}]_{\text{Sq}(z)}^{t_e}} = [X_+^{(\text{dc})}]_{|0} \mathcal{F}_0(z, \Lambda). \quad (\text{J17})$$

Since  $|\mathcal{F}_0(z, \Lambda)| < 1$ , this  $t_e$ -independent measurement is lower than the one when only vacuum injected in the radiation channel. It also represents the average contrast for Levitons of width  $\tau_e$  injected at random emission and it is lower than the vacuum baseline. This is the effect of the average number of photons in a squeezed vacuum given by Eq. (J8).

### Appendix K: Single EMP detection

We now discuss the evaluation of the parameter  $x(t) = 2\pi |\langle \chi | S_{ba}^* \Lambda_t \rangle|^2$  that appears in the evaluation of the Franck-Condon factor for Fock states (see Eq. (48)). The qualitative behavior of this quantity can be understood by using a time/frequency representation of the current noise. The case of a narrow band EMP then leads to analytical approximated expressions for  $x(t)$ .

### 1. Time frequency analysis of current noise

Using  $\hat{v}(\omega) = -e\sqrt{\omega} b(\omega)$  ( $\omega > 0$ ) for a single chiral integer quantum Hall edge channel,  $x(t) = 2\pi |\langle \chi | S_{ba}^* \Lambda_t \rangle|^2$  can be expressed in terms of the excess current noise  $\Delta S_{|1;\chi}^{(i)}(t, t')$  of a single quantum EMP in the mode  $\chi$ :

$$x(t) = \frac{2\pi^2}{e^2} \int_{\mathbb{R}^2} \Gamma_{ba}(t-t_+) \Gamma_{ba}(t-t_-)^* \Delta S_{|1;\chi}^{(i)}(t_+, t_-) dt_+ dt_- \quad (\text{K1})$$

in which  $\Gamma_{ba}$  denotes the function defined by Eq. (F2). The physical meaning of this expression is better understood in terms of the Wigner function  $\Delta W_{\rho}^{(i)}(t, \omega)$  of the excess current noise

$$\Delta W_{\rho}^{(i)}(t, \omega) = \int_{\mathbb{R}} \left\langle : \hat{v}\left(t - \frac{\tau}{2}\right) \hat{v}\left(t + \frac{\tau}{2}\right) : \right\rangle_{\rho, c} e^{i\omega\tau} d\tau \quad (\text{K2})$$

in which  $\langle AB \rangle_c$  denotes the connected correlator  $\langle AB \rangle - \langle A \rangle \langle B \rangle$ . Introducing the Ville transform associated with  $\Gamma_{ba}(t)$ :

$$W_{\Gamma_{ba}}(t, \omega) = \int_{\mathbb{R}} \Gamma_{ba}\left(t + \frac{\tau}{2}\right) \Gamma_{ba}\left(t - \frac{\tau}{2}\right) e^{i\omega\tau} d\tau. \quad (\text{K3})$$

leads to

$$x(t) = \frac{2\pi^2}{e^2} \int_{\mathbb{R}^2} W_{\Gamma_{ba}}(t - \tau, \omega) \Delta W_{|1;\chi}^{(i)}(\tau, \omega) \frac{d\omega d\tau}{2\pi}. \quad (\text{K4})$$

This shows that the radiation coupler's response function  $\Gamma_{ba}(\tau)$  leads to time-frequency filtering of the excess quantum current noise of the single EMP state  $|1, \chi\rangle$ . The time resolution for single EMP detection is thus limited by the duration of the excess current noise associated with the single EMP as well as by the response time of the radiation coupler, typically the  $RC$ -time scale appearing in  $\Gamma_{ba}$  (see Appendix F).

### 2. Current noise of a single EMP

For the single plasmon with wave-function  $\chi$ , the average excess current  $\langle i(t) \rangle_{|1;\chi}$  is zero and the Wigner function of the excess current noise defined in Eq. (K2) is given by

$$\begin{aligned} \Delta W_{|1;\chi}^{(i)}(t, \omega) &= \frac{e^2}{2\pi} \int_{|\Omega| \leq 2|\omega|} e^{-i\Omega t} \sqrt{\omega^2 - \frac{\Omega^2}{4}} \\ &\times \chi\left(|\omega| + \frac{\Omega}{2}\right) \chi\left(|\omega| - \frac{\Omega}{2}\right)^* \frac{d\Omega}{2\pi}. \end{aligned} \quad (\text{K5a})$$

In the case of a narrowband single plasmon centered at the energy  $\hbar\omega_0$  with Lorentzian linewidth  $\gamma_0$

$$\chi(\omega) = \frac{\sqrt{\gamma_0} \Theta(\omega)}{\omega - \omega_0 + \frac{i\gamma_0}{2}}. \quad (\text{K6})$$

such that  $\gamma_0 \ll \omega_0$ , the Wigner function of the excess current noise can be approximated by the usual expression for such energy resolved excitations:

$$\Delta W_{|1;\chi\rangle}^{(i)}(t, \omega) \simeq \Theta(t) \frac{e^2 \omega_0}{2\pi} 4\gamma_0 t \operatorname{sinc}(2(|\omega| - \omega_0)t) e^{-\gamma_0 t}. \quad (\text{K7})$$

The general expression of the heat current  $\mathcal{J}_Q(t)$  in terms of the current  $i(t)$  leads to

$$\langle \mathcal{J}_Q(t) \rangle_\rho = \frac{R_K}{2} \left( \langle i(t) \rangle_\rho^2 + \int_{\mathbb{R}} \Delta W_\rho^{(i)}(t, \omega) \frac{d\omega}{2\pi} \right). \quad (\text{K8})$$

For a single energy resolved EMP with energy  $\hbar\omega_0$  and Lorentzian lineshape of width  $\gamma_0$ , this enables us to compute the instantaneous heat current just from the excess noise since  $\langle i(t) \rangle_{|1;\chi\rangle} = 0$ . Using Eq. (K7), we find:

$$\langle \mathcal{J}_Q(t) \rangle_{|1;\chi\rangle} = \hbar\omega_0 \Theta(t) \gamma_0 e^{-\gamma_0 t}. \quad (\text{K9})$$

This heat current carries an average energy  $\int_{\mathbb{R}} \langle \mathcal{J}_Q(t) \rangle_{|1;\chi\rangle} dt = \hbar\omega_0$  as expected.

### 3. Filtering of current noise

If the EMP has a narrow band compared to the typical scale of variation of  $\Gamma_{ba}(\omega)$ , the variation of  $S_{ba}(\omega)$  around  $\omega_0$  can be neglected in Eq. (49). One then recognizes in  $x(t)$  the modulus square

$$\frac{e^2}{2\pi} \left| \int_0^{+\infty} \sqrt{\omega} \chi(\omega) e^{-i\omega t} \frac{d\omega}{\sqrt{2\pi}} \right|^2 = \int_{\mathbb{R}} \Delta W_{|1;\chi\rangle}^{(i)}(t, \omega) \frac{d\omega}{2\pi} \quad (\text{K10})$$

where the r.h.s. directly follows from Eq. (K5). Eq. (K8) then shows that this is related to the average instantaneous heat current carried by the single EMP in state  $\chi$ . This finally leads to Eq. (50).

- 
- [1] G. Fève, A. Mahé, J. Berroir, T. Kontos, B. Plaçais, D. C. Glattli, A. Cavanna, B. Etienne, and Y. Jin, An on-demand single electron source, *Science* **316**, 1169 (2007).
  - [2] J. Dubois, T. Jullien, F. Portier, P. Roche, A. Cavanna, Y. Jin, W. Wegscheider, P. Rouleau, and D. C. Glattli, Minimal excitation states for electron quantum optics using Levitons, *Nature* **502**, 659 (2013).
  - [3] E. Bocquillon, V. Freulon, F. Parmentier, J.-M. Berroir, B. Plaçais, C. Wahl, J. Rech, T. Jonckheere, T. Martin, C. Grenier, D. Ferraro, P. Degiovanni, and G. Fève, Electron quantum optics in ballistic chiral conductors, *Ann. Phys. (Berlin)* **526**, 1 (2014).
  - [4] E. Bocquillon, F. Parmentier, C. Grenier, J.-M. Berroir, P. Degiovanni, D. Glattli, B. Plaçais, A. Cavanna, Y. Jin, and G. Fève, Electron quantum optics: partitioning electrons one by one, *Phys. Rev. Lett.* **108**, 196803 (2012).
  - [5] E. Bocquillon, V. Freulon, J.-M. Berroir, P. Degiovanni, B. Plaçais, A. Cavanna, Y. Jin, and G. Fève, Coherence and indistinguishability of single electrons emitted by independent sources, *Science* **339**, 1054 (2013).
  - [6] A. Marguerite, C. Cabart, C. Wahl, B. Roussel, V. Freulon, D. Ferraro, C. Grenier, J. M. Berroir, B. Plaçais, T. Jonckheere, J. Rech, T. Martin, P. Degiovanni, A. Cavanna, Y. Jin, and G. Fève, Decoherence and relaxation of a single electron in a one-dimensional conductor, *Phys. Rev. B* **94**, 115311 (2016).
  - [7] P. Rouleau, F. Portier, P. Roche, A. Cavanna, G. Faini, U. Gennser, and D. Mailly, Direct measurement of the coherence length of edge states in the integer quantum Hall regime, *Phys. Rev. Lett.* **100**, 126802 (2008).
  - [8] P. Rouleau, F. Portier, P. Roche, A. Cavanna, G. Faini, U. Gennser, and D. Mailly, Tuning decoherence with a voltage probe, *Phys. Rev. Lett.* **102**, 236802 (2009).
  - [9] S. Tewari, P. Rouleau, C. Grenier, F. Portier, A. Cavanna, U. Gennser, D. Mailly, and P. Roche, Robust quantum coherence above the Fermi sea, *Phys. Rev. B* **93**, 035420 (2016).
  - [10] R. Rodriguez, F. Parmentier, D. Ferraro, P. Rouleau, U. Gensser, A. Cavanna, M. Sasseti, F. Portier, D. Mailly, and P. Roche, Relaxation and revival of quasi-particles injected in an interacting quantum Hall liquid, *Nature Communications* **11**, 2426 (2020).
  - [11] M. Jo, J.-Y. M. Lee, A. Assouline, P. Brasseur, K. Watanabe, T. Taniguchi, P. Roche, D. C. Glattli, N. Kumada, F. D. Parmentier, H. S. Sim, and P. Rouleau, Scaling behavior of electron decoherence in a graphene Mach-Zehnder interferometer, *Nature Communications* **13**, 5473 (2022).
  - [12] R. Bisognin, A. Marguerite, B. Roussel, M. Kumar, C. Cabart, C. Chapdelaine, A. Mohammad-Djafari, J. M. Berroir, E. Bocquillon, B. Plaçais, A. Cavanna, U. Gennser, Y. Jin, P. Degiovanni, and G. Fève, Quantum tomography of electrical currents, *Nature Communications* **10**, 3379 (2019).
  - [13] V. Kashcheyevs, P. Degiovanni, B. Roussel, M. Kataoka, J. D. Fletcher, L. Freise, N. Ubbelhode, G. Fève, H. Bartolomei, F. Couëdo, A. Kadykov, W. Poirier, P. Rouleau, F. D. Parmentier, and F. Hohls, Single-electron wave packets for quantum metrology: concepts, implementations and applications (2021), SEQUOIA project (17FUN04) technical report.
  - [14] M. Aluffi, T. Vasselon, S. Ouacel, H. Edlbauer, C. Geffroy, P. Rouleau, D. C. Glattli, G. Georgiou, and C. Bäuerle, Ultrashort electron wave packets via frequency-comb synthesis, *Phys. Rev. Appl.* **20**, 034005 (2023).
  - [15] D. Glattli, J. Nath, I. Taktak, P. Rouleau, C. Bauerle, and X. Waintal, Design of a single-shot electron detector with sub-electron sensitivity for electron flying qubit operation (2020), arXiv:2002.03947.
  - [16] A. Blais, A. L. Grimsmo, S. M. Girvin, and A. Wallraff, Circuit quantum electrodynamics, *Rev. Mod. Phys.* **93**, 025005 (2021).
  - [17] G. Burkard, T. D. Ladd, A. Pan, J. M. Nichol, and J. R. Petta, Semiconductor spin qubits, *Rev. Mod. Phys.* **95**, 025003 (2023).

- [18] H. Edlbauer, J. Wang, T. Crozes, P. Perrier, S. Ouacel, C. Geffroy, G. Georgiou, E. Chatzikyriakou, A. Lacerda-Santos, X. Waintal, D. C. Glatli, P. Rouleau, J. Nath, M. Kataoka, J. Splettstoesser, M. Acciai, M. C. da Silva Figueira, K. Öztas, A. Trelakis, T. Grange, O. M. Yevtushenko, S. Birner, and C. Bäuerle, Semiconductor-based electron flying qubits: review on recent progress accelerated by numerical modelling, *EPJ Quantum Technology* **9**, 21 (2022).
- [19] L. Viti and M. S. Vitiello, Tailored nano-electronics and photonics with two-dimensional materials at terahertz frequencies, *Journal of Applied Physics* **130**, 170903 (2021).
- [20] A. Facon, E.-K. Dietsche, D. Grosso, S. Haroche, J.-M. Raimond, M. Brune, and S. Gleyzes, A sensitive electrometer based on a Rydberg atom in a Schrödinger-cat state, *Nature* **535**, 262 (2016).
- [21] V. Calero, M. A. Suarez, R. Salut, F. Baida, A. Caspar, F. Behague, N. Courjal, L. Galtier, L. Gillette, L. Duvillaret, G. Gaborit, and M. P. Bernal, An ultra wideband-high spatial resolution-compact electric field sensor based on lab-on-fiber technology, *Scientific Reports* **9**, 8058 (2019).
- [22] A. N. Cleland and M. L. Roukes, A nanometre-scale mechanical electrometer, *Nature* **392**, 160 (1998).
- [23] D. Chen, H. Zhang, J. Sun, M. Pandit, G. Sobreviela, Y. Wang, Q. Zhang, X. Chen, A. Seshia, and J. Xie, Ultrasensitive resonant electrometry utilizing micromechanical oscillators, *Phys. Rev. Applied* **14**, 014001 (2020).
- [24] I. Ahmed, J. A. Haigh, S. Schaal, S. Barraud, Y. Zhu, C.-m. Lee, M. Amado, J. W. A. Robinson, A. Rossi, J. J. L. Morton, and M. F. Gonzalez-Zalba, Radio-frequency capacitive gate-based sensing, *Phys. Rev. Applied* **10**, 014018 (2018).
- [25] F. Dolde, M. W. Doherty, J. Michl, I. Jakobi, B. Naydenov, S. Pezzagna, J. Meijer, P. Neumann, F. Jelezko, N. B. Manson, and J. Wrachtrup, Nanoscale detection of a single fundamental charge in ambient conditions using the NV<sup>-</sup> center in diamond, *Phys. Rev. Lett.* **112**, 097603 (2014).
- [26] A. N. Vamivakas, Y. Zhao, S. Fält, A. Badolato, J. M. Taylor, and M. Atatüre, Nanoscale optical electrometer, *Phys. Rev. Lett.* **107**, 166802 (2011).
- [27] C. Arnold, V. Loo, A. Lemaître, I. Sagnes, O. Krebs, P. Voisin, P. Senellart, and L. Lanco, Cavity-enhanced real-time monitoring of single-charge jumps at the microsecond time scale, *Phys. Rev. X* **4**, 021004 (2014).
- [28] H. Brenning, S. Kafanov, T. Duty, S. Kubatkin, and P. Delsing, An ultrasensitive radio-frequency single-electron transistor working up to 4.2 K, *Journal of Applied Physics* , 114321 (2006).
- [29] D. J. Reilly, C. M. Marcus, M. P. Hanson, and A. C. Gossard, Fast single-charge sensing with a rf quantum point contact, *Applied Physics Letters* **91**, 162101 (2007).
- [30] M. Hatridge, R. Vijay, D. H. Slichter, J. Clarke, and I. Siddiqi, Dispersive magnetometry with a quantum limited squid parametric amplifier, *Phys. Rev. B* **83**, 134501 (2011).
- [31] M. J. Biercuk, D. J. Reilly, T. M. Buehler, V. C. Chan, J. M. Chow, R. G. Clark, and C. M. Marcus, Charge sensing in carbon-nanotube quantum dots on microsecond timescales, *Phys. Rev. B* **73**, 201402 (2006).
- [32] Y. Ji, Y. Chung, D. Sprinzak, M. Heiblum, D. Mahalu, and H. Shtrikman, An electronic mach-zehnder interferometer, *Nature* **422**, 415 (2003).
- [33] J. R. Souquet, M. J. Woolley, J. Gabelli, P. Simon, and A. A. Clerk, Photon-assisted tunnelling with nonclassical light, *Nature Communications* **5**, 5562 (2014).
- [34] C. Guerlin, J. Bernu, S. Deléglise, C. Sayrin, S. Gleyzes, S. Kuhr, M. Brune, J.-M. Raimond, and S. Haroche, Progressive field-state collapse and quantum non-demolition photon counting, *Nature* **448**, 889 (2007).
- [35] V. B. Braginsky, Y. Vorontsov, and K. Thorne, Quantum nondemolition measurements, *Science* **209**, 547 (1980).
- [36] T. Jullien, P. Rouleau, P. Roche, A. Cavanna, Y. Jin, and D. C. Glatli, Quantum tomography of an electron, *Nature* **514**, 603 (2014).
- [37] J. D. Fletcher, N. Johnson, E. Locane, P. See, J. P. Griffiths, I. Farrer, D. A. Ritchie, P. W. Brouwer, V. Kashcheyevs, and M. Kataoka, Continuous-variable tomography of solitary electrons, *Nature Communications* **10**, 5298 (2019).
- [38] B. Roussel, C. Cabart, G. Fève, and P. Degiovanni, Processing quantum signals carried by electrical currents, *Physical Review X Quantum* **2**, 020314 (2021).
- [39] F. Hohls, A. C. Welker, C. Leicht, L. Fricke, B. Kaestner, P. Mirovsky, A. Müller, K. Pierz, U. Siegner, and H. W. Schumacher, Semiconductor quantized voltage source, *Phys. Rev. Lett.* **109**, 056802 (2012).
- [40] J. D. Fletcher, P. See, H. Howe, M. Pepper, S. P. Giblin, J. P. Griffiths, G. A. C. Jones, I. Farrer, D. A. Ritchie, T. J. B. M. Janssen, and M. Kataoka, Clock-controlled emission of single-electron wave packets in a solid-state circuit, *Phys. Rev. Lett.* **111**, 216807 (2013).
- [41] J. Waldie, P. See, V. Kashcheyevs, J. P. Griffiths, I. Farrer, G. A. C. Jones, D. A. Ritchie, T. J. B. M. Janssen, and M. Kataoka, Measurement and control of electron wave packets from a single-electron source, *Phys. Rev. B* **92**, 125305 (2015).
- [42] G. Roussely, E. Arrighi, G. Georgiou, S. Takada, M. Schalk, M. Urdampilleta, A. Ludwig, A. D. Wieck, P. Armagnat, T. Kloss, X. Waintal, T. Meunier, and C. Bäuerle, Unveiling the bosonic nature of an ultrashort few-electron pulse, *Nature Communications* **9**, 2811 (2018).
- [43] A. Assouline, L. Pugliese, H. Chakraborti, S. Lee, L. Bernabeu, M. Jo, K. Watanabe, T. Taniguchi, D. C. Glatli, N. Kumada, H.-S. Sim, F. D. Parmentier, and P. Rouleau, Emission and coherent control of levitons in graphene, *Science* **382**, 1260 (2023).
- [44] D. Ferraro, B. Roussel, C. Cabart, E. Thibierge, G. Fève, C. Grenier, and P. Degiovanni, Real-time decoherence of Landau and Levitov quasiparticles in quantum Hall edge channels, *Phys. Rev. Lett.* **113**, 166403 (2014).
- [45] C. Cabart, B. Roussel, G. Fève, and P. Degiovanni, Taming electronic decoherence in 1d chiral ballistic quantum conductors, *Phys. Rev. B* **98**, 155302 (2018).
- [46] E. Condon, A theory of intensity distribution in band systems, *Phys. Rev.* **28**, 1182 (1926).
- [47] I. Safi and H. J. Schulz, Transport in an inhomogeneous interacting one-dimensional system, *Phys. Rev. B* **52**, R17040 (1995).
- [48] I. Safi, A dynamic scattering approach for a gated interacting wire, *Eur. Phys. J. D* **12**, 451 (1999).



- [49] D. Ferraro, F. Ronetti, J. Rech, T. Jonckheere, M. Sasseti, and T. Martin, Enhancing photon squeezing one Leviton at a time, *Phys. Rev. B* **97**, 155135 (2018).
- [50] G. Rebora, D. Ferraro, and M. Sasseti, Suppression of the radiation squeezing in interacting quantum Hall edge channels, *New Journal of Physics* **23**, 063018 (2021).
- [51] H. Bartolomei, R. Bisognin, H. Kamata, J.-M. Berroir, E. Bocquillon, G. Ménard, B. Plaçais, A. Cavanna, U. Gennser, Y. Jin, P. Degiovanni, C. Mora, and G. Fève, Observation of edge magnetoplasmon squeezing in a quantum hall conductor, *Phys. Rev. Lett.* **130**, 106201 (2023).
- [52] G. Gasse, C. Lupien, and B. Reulet, Observation of squeezing in the electron quantum shot noise of a tunnel junction, *Phys. Rev. Lett.* **111**, 136601 (2013).
- [53] U. Mendes and C. Mora, Cavity squeezing by a quantum conductor, *New Journal of Physics* **17**, 11 (2015).
- [54] M. Moskalets and M. Büttiker, Floquet scattering theory for current and heat noise in large amplitude adiabatic pumps, *Phys. Rev. B* **70**, 245305 (2004).
- [55] N. Ubbelohde, L. Freise, E. Pavlovska, P. G. Silvestrov, P. Recher, M. Kokainis, G. Barinovs, F. Hohls, T. Weimann, K. Pierz, and V. Kashcheyevs, Two electrons interacting at a mesoscopic beam splitter, *Nature Nanotechnology* **18**, 733 (2023).
- [56] A. C. Elitzur and L. Vaidman, Quantum mechanical interaction-free measurements, *Foundations of Physics* **23**, 987 (1993).
- [57] I. Safi and H. Schulz, Transport through a single band wire connected to measuring leads, in *Quantum Transport in Semiconductor Submicron Structures*, edited by B. Kramer (Kluwer Academic Press, Dordrecht, 1995) p. 159.
- [58] P. Degiovanni, C. Grenier, and G. Fève, Decoherence and relaxation of single electron excitations in quantum Hall edge channels, *Phys. Rev. B* **80**, 241307(R) (2009).
- [59] P. Degiovanni, C. Grenier, G. Fève, C. Altimiras, H. le Sueur, and F. Pierre, Plasmon scattering approach to energy exchange and high-frequency noise in  $\nu = 2$  quantum Hall edge channels, *Phys. Rev. B* **81**, 121302(R) (2010).
- [60] E. Bocquillon, V. Freulon, J.-M. Berroir, P. Degiovanni, B. Plaçais, A. Cavanna, Y. Jin, and G. Fève, Separation between neutral and charge modes in one dimensional chiral edge channels, *Nature Communications* **4**, 1839 (2013).
- [61] P. Woodward, *Probability and information theory, with applications to radar* (McGraw-Hill, New York, 1953).
- [62] J. Chalker, Y. Gefen, and M. Veillette, Decoherence and interactions in an electronic Mach-Zehnder interferometer, *Phys. Rev. B* **76**, 085320 (2007).
- [63] I. Levkivskyi and E. Sukhorukov, Dephasing in the electronic Mach-Zehnder interferometer at filling factor  $\nu = 2$ , *Phys. Rev. B* **78**, 045322 (2008).
- [64] C. Neuenhahn and F. Marquardt, Dephasing by electron-electron interactions in a ballistic interferometer, *New Journal of Physics* **10**, 115018 (2008).
- [65] C. Neuenhahn and F. Marquardt, Universal dephasing in a chiral 1d interacting Fermion system, *Phys. Rev. Lett.* **102**, 046806 (2009).
- [66] C. Grenier, R. Hervé, G. Fève, and P. Degiovanni, Electron quantum optics in quantum Hall edge channels, *Mod. Phys. Lett. B* **25**, 1053 (2011), proceedings of the Statphys 24 satellite meeting "International Conference on Frustrated Spin Systems, Cold Atoms and Nanomaterials" (Hanoi, 14-16 July 2010).
- [67] G. Rebora, D. Ferraro, R. H. Rodriguez, F. D. Parmentier, P. Roche, and M. Sasseti, Electronic wave-packets in integer quantum Hall edge channels: Relaxation and dissipative effects, *Entropy* **23**, 10.3390/e23020138 (2021).
- [68] K. S. Singwi and A. Sjölander, Resonance absorption of nuclear gamma rays and the dynamics of atomic motions, *Phys. Rev.* **120**, 1093 (1960).
- [69] C. Tzara, Diffusion des photons sur les atomes et les noyaux dans les cristaux, *J. Phys. Radium* **22**, 303 (1961).
- [70] D. Dasenbrook and C. Flindt, Dynamical scheme for interferometric measurements of full-counting statistics, *Phys. Rev. Lett.* **117**, 146801 (2016).
- [71] J. Dubois, T. Jullien, C. Grenier, P. Degiovanni, P. Roulleau, and D. C. Glattli, Integer and fractional charge lorentzian voltage pulses analyzed in the framework of photon-assisted shot noise, *Phys. Rev. B* **88**, 085301 (2013).
- [72] E. G. Idrisov, I. P. Levkivskyi, and E. V. Sukhorukov, Dephasing in a Mach-Zehnder interferometer by an ohmic contact, *Phys. Rev. Lett.* **121**, 026802 (2018).
- [73] H. Duprez, E. Sivre, A. Anthore, A. Aassime, A. Cavanna, U. Gennser, and F. Pierre, Transmitting the quantum state of electrons across a metallic island with coulomb interaction, *Science* **366**, 1243 (2019).
- [74] M. Misiorny, G. Fève, and J. Splettstoesser, Shaping charge excitations in chiral edge states with a time-dependent gate voltage, *Phys. Rev. B* **97**, 075426 (2018).
- [75] H. Duprez, E. Sivre, A. Anthore, A. Aassime, A. Cavanna, A. Ouerghi, U. Gennser, and F. Pierre, Macroscopic electron quantum coherence in a solid-state circuit, *Phys. Rev. X* **9**, 021030 (2019).
- [76] This is justified by observing that  $S_{ba}(\omega_0)^2/\mathcal{Q}_0$  is significantly smaller than unity and experimentally achieved squeezing parameters are below  $z \simeq 0.0719$ . Even a 3 dB noise reduction corresponds to  $z \simeq 0.1733$ .
- [77] The only hypothesis for deriving Eqs. (50) and (52) is that  $|S_{ba}(\omega)|^2$  does not vary significantly on the bandwidth of  $\chi$ .
- [78] B. I. Halperin, A. Stern, I. Neder, and B. Rosenow, Theory of the Fabry-Pérot quantum Hall interferometer, *Phys. Rev. B* **83**, 155440 (2011).
- [79] G. A. Frigeri, D. D. Scherer, and B. Rosenow, Subperiods and apparent pairing in integer quantum Hall interferometers, *Europhysics Letters* **126**, 67007 (2019).
- [80] G. A. Frigeri and B. Rosenow, Electron pairing in the quantum Hall regime due to neutralon exchange, *Phys. Rev. Res.* **2**, 043396 (2020).
- [81] C. Bauerle, D. Glattli, T. Meunier, F. Portier, P. Roche, P. Roulleau, S. Takada, and X. Waintal, Coherent control of single electrons: a review of current progress, *Reports on Progress in Physics* **81**, 056503 (2018).
- [82] H. Souquet-Basiège, B. Roussel, G. Rebora, G. Ménard, I. Safi, G. Fève, and P. Degiovanni, The electronic ambiguity function in single electron interferometry (2024), en preparation.
- [83] J. R. Klauder, A. C. Price, S. Darlington, and W. J. Albersheim, The theory and design of chirp radars, *The Bell system Technical Journal* **34**, 745 (1960).

- [84] J. Radon, On the determination of functions from their integral values along certain manifolds, *IEEE Transactions on Medical Imaging* **5**, 170 (1986).
- [85] D. T. Smithey, M. Beck, M. G. Raymer, and A. Fardani, Measurement of the Wigner distribution and the density matrix of a light mode using optical homodyne tomography: Application to squeezed states and the vacuum, *Phys. Rev. Lett.* **70**, 1244 (1993).
- [86] A. I. Lvovsky and M. G. Raymer, Continuous-variable optical quantum-state tomography, *Rev. Mod. Phys.* **81**, 299 (2009).
- [87] M. Tsang, R. Nair, and X.-M. Lu, Quantum theory of superresolution for two incoherent optical point sources, *Phys. Rev. X* **6**, 031033 (2016).
- [88] M. Tsang, Subdiffraction incoherent optical imaging via spatial-mode demultiplexing, *New Journal of Physics* **19**, 023054 (2017).
- [89] J. Řeháček, Z. Hradil, B. Stoklasa, M. Paúr, J. Grover, A. Krzic, and L. L. Sánchez-Soto, Multiparameter quantum metrology of incoherent point sources: Towards realistic superresolution, *Phys. Rev. A* **96**, 062107 (2017).
- [90] M. Paúr, B. Stoklasa, J. Grover, A. Krzic, L. L. Sánchez-Soto, Z. Hradil, and J. Řeháček, Tempering Rayleigh curse with psf shaping, *Optica* **5**, 1177 (2018).
- [91] F. Benatti, R. Floreanini, and U. Marzolino, Entanglement in Fermion systems and quantum metrology, *Phys. Rev. A* **89**, 032326 (2014).
- [92] V. Giovannetti, S. Lloyd, and L. Maccone, Advances in quantum metrology, *Nat Photon* **5**, 222 (2011).
- [93] L. Freise, T. Gerster, D. Reifert, T. Weimann, K. Pierz, F. Hohls, and N. Ubbelohde, Trapping and counting ballistic nonequilibrium electrons, *Phys. Rev. Lett.* **124**, 127701 (2020).
- [94] V. Thiney, P.-A. Mortemousque, K. Rogdakis, R. Thalineau, A. Ludwig, A. D. Wieck, M. Urdampilleta, C. Bäuerle, and T. Meunier, In-flight detection of few electrons using a singlet-triplet spin qubit, *Phys. Rev. Res.* **4**, 043116 (2022).
- [95] M. Büttiker, A. Prêtre, and H. Thomas, Dynamic conductance and the scattering matrix of small conductors, *Phys. Rev. Lett.* **70**, 4114 (1993).
- [96] The radius one reflects the relaxation resistance  $R_q = R_K/2$  of the circuit predicted in Ref. [107].
- [97] A. Delgard, B. Chenaud, U. Gennser, A. Cavanna, D. Mailly, P. Degiovanni, and C. Chaubet, Coulomb interactions and effective quantum inertia of charge carriers in a macroscopic conductor, *Phys. Rev. B* **104**, L121301 (2021).
- [98] A. Delgard, B. Chenaud, U. Gennser, A. Cavanna, D. Mailly, P. Degiovanni, and C. Chaubet, Supplementary material (Detailed computations and complementary experimental results) (2021).
- [99] C. Grenier, R. Hervé, E. Bocquillon, F. Parmentier, B. Plaçais, J.-M. Berroir, G. Fève, and P. Degiovanni, Single electron quantum tomography in quantum Hall edge channels, *New Journal of Physics* **13**, 093007 (2011).
- [100] We will discuss other cases later but for the average current, any other contribution would be irrelevant.
- [101] D. Ferraro, C. Wahl, J. Rech, T. Jonckheere, and T. Martin, Electronic Hong-Ou-Mandel interferometry in two-dimensional topological insulators, *Phys. Rev. B* **89**, 075407 (2014).
- [102] D. Dasenbrook, J. Bowles, J. B. Brask, P. P. Hofer, C. Flindt, and N. Brunner, Single-electron entanglement and nonlocality, *New Journal of Physics* **18**, 043036 (2016).
- [103] The truncation for positive or negative energies can be neglected provided  $\gamma_e \ll |\omega_e|$ .
- [104] C. Grenier, J. Dubois, T. Jullien, P. Roulleau, D. C. Glattli, and P. Degiovanni, Fractionalization of minimal excitations in integer quantum Hall edge channels, *Phys. Rev. B* **88**, 085302 (2013).
- [105] Note that  $|S_{q_0}\rangle = |0\rangle$ .
- [106] G. Rebora, B. Roussel, G. Fève, I. Safi, and P. Degiovanni, in preparation.
- [107] M. Büttiker, H. Thomas, and A. Prêtre, Mesoscopic capacitors, *Phys. Lett. A* **180**, 364 (1993).